Linking biological and physical aging: Dynamical scaling of multicellular regeneration

Yuting Lou,[1] Jufeng Xia,[2] Wei Tang,[2] and Yu Chen[1]

[1]*SCS Lab, Department of Human and Environmental Engineering, Graduate School of Frontier Sciences,*
The University of Tokyo, Chiba, Japan
[2]*Hepato-Biliary-Pancreas Lab, Division of Surgery, Graduate School of Medicine, The University of Tokyo, Tokyo, Japan*

The fight against biological aging (bio-aging) is long-standing, with the focus of intense research aimed at maintaining high rates of tissue regeneration to promote health and longevity. Nevertheless, there are overwhelming complexities associated with the quantitative analysis of aging. In this study, we sought to quantify bio-aging based on physical aging, by mapping instances of multicellular regeneration to the relaxation of physical systems. An experiment of delayed wound healing assays was devised to obtain delay-dependent healing data. The experiment confirmed the slowdown of healing events, which fitted dynamical scaling just as relaxation events do in physical aging. The scaling exponent, which describes the aging rate in physics, is here similarly proposed as an indicator of the deterioration rate of tissue-regenerative power. Parallel equation-based and cell-based simulations also revealed that asymmetric cell cycle-regulatory mechanisms under strong growth-inhibitory conditions predominantly control the critical slowdown of healing analogous to physical criticality. By establishing a direct link between physical aging and biological aging, we are able to estimate the aging rate of tissues and to achieve an integrated understanding of bio-aging mechanism which may improve the modulation of regeneration for clinical use.

I. INTRODUCTION

Aging prevention has been a focus for humans for decades. Most mammalian tissues lose the capacity to regenerate with age, and this deterioration severely affects health and longevity [1]. Numerous aging studies have attributed this lost capacity for repair to shortening of telomeres, deterioration of the extracellular niche, or intrinsically blunted regulation of key molecules [2–7]. This inconsistency in terms of the probable causes of aging has made it difficult to pinpoint how and why the body ages. If we are to generate better antiaging therapies, an integrated theory of biological aging (bio-aging) is in demand, despite the tough challenges in the quantification of aging events and in the clarification of the governing factors.

Unlike the ambiguously defined aging of biological systems, aging of physical systems has an explicit definition and has been quantified in diverse complex soft materials from glasses to cytoskeletons [8–12]. This ubiquitous phenomenon of losing the relaxation ability over time in multiparticle systems can be expressed in mathematical equations: e.g., for systems prepared in a nonequilibrium state, the relaxation processes probed at different times feature *dynamical scaling*, indicating a slowdown of the system dynamics as if the system were aging [13,14]. Such physical aging originates from the ergodicity breaking of the dynamics [15], and this nonergodicity is a more typical feature of complex living systems. Recent research suggests that the nonequilibrium physics of glass or jamming transition is exhibited in confluent cell layers [16–23]. In this study, we sought to advance this idea and investigate a more complicated biophenomenon: the multicellular regeneration. Regeneration is a renewal process of a structurally damaged multicellular system such as tissues and organs, and involves not only mechanical but also biochemical processes related to cell cycle, intercellular signaling, and cell-microenvironment interactions among others [24]. We define the bio-aging (especially the tissue aging) as the process

of losing the capacity for regeneration and attempt to attain an integrated theory of it via the mapping between regeneration and physical relaxation.

Multicellular regeneration can be explored with a wound healing assay (WHA) [25–27], which is a simple and inexpensive *in vitro* experiment used for scrutinizing the coordinated cell proliferation and migration in tissue regeneration or tumor invasion. In WHAs, "wound healing" refers to the event that a sheet of cells regenerates to form a confluent monolayer again after some cells have been removed. Just as *relaxation* is the collective response of particles to an external perturbation in physics, *healing* is the collective response of cells to an external damage (the wound) and hence it can be regarded as an analog of relaxation in biology.

Conventional WHAs require wounds to be performed immediately after cell starvation to avoid any changes in cellular conditions that may occur over time. However, our study focuses on the very poststarvation alterations in cellular conditions. Thus, we devised a time-delayed WHA (TDWHA), in which wound creation is delayed for a specific time (defined as "waiting time"; Fig. 1). With all the other experimental settings identical, the relation between the waiting time and the healing event can characterize the endogenous evolution of the system. In particular, a slowdown of healing with the increasing waiting time is suggestive of the existence of bio-aging.

In Sec. II, we introduce the experimental settings and the results of TDWHAs. Basically, we found that the healing events as a function of the waiting times exhibit *dynamical scaling* just as the relaxations do in physical aging. In Secs. III and IV, we evaluate the role of multiple factors such as contact inhibition, cell proliferation, cell migration, extracellular matrix (ECM), and cell cycle regulation using a minimal equation-based model in parallel with an agent-based model. We identified in both models the parameter which governs the *dynamical scaling* of healing and also investigated
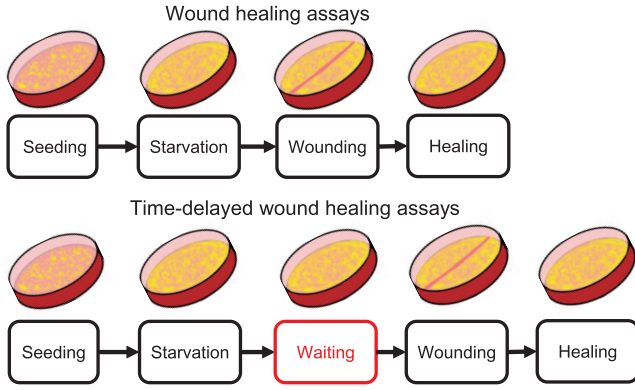
FIG. 1. Procedures in wound healing assays (top) and time-delayed wound healing assays (bottom). In the time-delayed wound healing assays, all the procedures are conducted as in the original assays except that the wounding operation is delayed for a specific time frame.
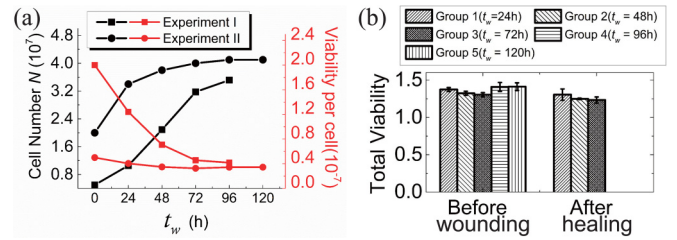

FIG. 2. Cell number and cell viability. (a) Variations in cell number (black), and average single cell viability (red) during natural growth before wounding. Cell number was counted with a hemocytometer as is described in Appendix A 2. Average single cell viability was calculated as the total cell viability divided by the cell number. Total cell viability was identified from 3-(4, 5-dimethylthiazol-2-yl)-2, 5-diphenyltetrazolium bromide (MTT) assays (see Appendix A 3), and all values are the ratio over the initial total cell viability immediately after starvation ($t = 0$). (b) Comparison of the total cell viability immediately before the wounding and after the completion of healing (in the first three groups only).

the corresponding criticality analogous to that in physical systems. A discussion of the analogy between multicellular regeneration and physical relaxation as well as its implication on the modulation of regeneration for clinical practices is provided in Sec. V. Section VI concludes the whole article.

II. TIME-DELAYED WOUND HEALING ASSAYS

A. Experiment settings

Newly thawed HepG2.2.15 cells were seeded near confluence into six-well plates at an initial density u_0, and the plates of cells were divided into N groups, of which 6–12 samples awaited wounding for an additional period of time $T_N = 24 \times N$ (h). After the creation of a 0.25-mm scratch wound, each group was continuously observed for ∼190 h and photographed once every 24 h. Two series of experiments were conducted with different initial seeding densities, $u_0 = 5 \times 10^5$ cells per mL in experiment I and $u_0 = 2 \times 10^6$ cells per mL in experiment II. To prevent biases among groups, we chose the HepG2.2.15 cell line, which features slow cell packing and low propensity to mutations. The microenvironment and experimental procedures were kept identical for all groups at all times for an exclusive examination of the time-dependent endogenous cellular changes (see Appendix A 1 for material and methods of the experiment).

B. Experiment results

1. Prewounding cell growth

Figure 2(a) shows the statistics of cell conditions before wounding in experiments I and II. An increase in the total cell number along with a decrease in the averaged single-cell viability can be observed (see Appendix A 2 and Appendix A 3 for the methods); for longer waiting times t_w (>72 h), the cell number and the single cell viability will approach a steady level, indicating the saturation of cell growth. Growth saturation in experiment II occurred earlier than in experiment I because of the higher seeding density. Figure 2(b) shows the total cell viability immediately before wounding and after the completion of healing in experiment II. Five groups exhibited almost the same level of viability before wounding. After

complete healing, the viability decreased in groups 1–3 within 5%, which is insignificant in comparison with the standard errors of 2% to 7%; this finding indicates that no metabolic deterioration occurred on the experimental time scale. With sufficient nutrients, the saturation of cell number and/or viability was most probably caused by density-dependent contact inhibition [28–34]. Increasing contact inhibition also relates to increased intercellular adhesion, which might induce irregular wound edge geometry that can affect the healing processes [35,36]. Nonetheless, it was later confirmed that this geometrical irregularity of edge did not bias the healing results (see Appendix D for an examination on the effects of edge geometries).

2. Postwounding healing

Figure 3 shows snapshots at three postwounding time points for four groups with waiting time t_w of 24, 48, 72, and 96 h. Groups with a longer waiting time exhibited slower healing, which is an indication of bio-aging. Through postprocessing of these snapshots, we can scrutinize this slowdown of healing from the perspectives of the healed area evolution and the density profile propagation.

The healed area ΔA is calculated as $\Delta A(t - t_w) = A(t_w) - A(t)$, where A is the wound area measured in the unit of 10^5 pixels from the snapshots (see detailed procedures in Appendix A 4). Figures 4(a1) and 4(b1) show the time evolution of ΔA in different groups, and the slope of the curves reflects the healing rate. The less steep healing curves with longer waiting times illustrate slower healing processes. From Fig. 2(a), the increasing density with waiting time seems to be the cause of slow healing for long waiting times. Nonetheless, healing events in experiment II [Fig. 4(b1)] progressed more quickly than those in experiment I [Fig. 4(a1)] for the correspondent groups because of a higher cell density, indicating that the increase in cell density contrarily promotes healing efficiency. Besides, by comparing group 3 in experiment I with group 1 in experiment II, we find that the group with a 72-h waiting time (in experiment I) healed much slower than the group with a 24-h waiting time (in experiment II), even
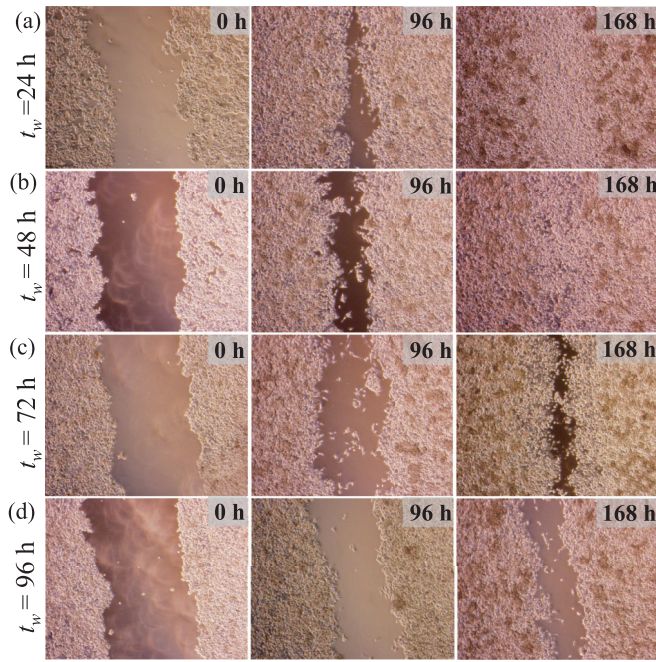
FIG. 3. Snapshots of 0, 96, and 168 h after the creation of the 0.25-mm scratch wound in time-delayed wound healing assays for HepG2.2.15 cells. (a) 24-h waiting time. (b) 48-h waiting time. (c) 72-h waiting time. (d) 96-h waiting time. The dark yellow clots scattered away from the wounds are packed cells.

though the two groups had similar prewounding cell densities (3.2×10^7 per well) [see Fig. 2(a)]. These comparisons confirm that the density effect is trivial compared with the aging effect brought by the waiting time. More importantly, if rescaling the time axis as $(t - t_w)/t_w{}^\mu$ where μ is a tunable scaling exponent, we further find that the data for all groups except for group1 ($t_w = 24$ h) collapsed to a single curve with $\mu = 0.72$, as shown in Figs. 4(a2) and 4(b2). The collapse of data on a rescaled time axis, known as *dynamical scaling*, prevails in physical aging. The exponent μ, termed as *aging exponent* [14], measures the rate of physical aging and we use it here to quantify the rate of bio-aging. A larger μ implies stronger aging, which can be interpreted as a rapid loss of capacity for healing. Last, the failure of rescaling in the data of group 1 in both experiments suggests that the onset of the dynamical scaling of aging took place after 48 h.

Meanwhile, as is observed in Fig. 3, a small number of cells migrated into the wound bed and the cell density is decreasing with the distance away from the original wound edge. We segmented the area around the wound edge into several bins of 25/3 microns width [Fig. 4(c1)] and constructed the profile of cell density in each sample snapshot by counting the area covered by the cells normalized by the total area in every bin. These profiles were further averaged for each bin over all samples with the same waiting time and the same postwounding time. Figure 4(c2) shows the evolution of average density profile as a function of the distance for group 1 ($t_w = 24$ h) and group 3 ($t_w = 72$ h) in experiment I, with the original wound edge (the half-density position immediately after wounding) calibrated to the zero point of the horizontal axis. We can observe that the postwounding average density
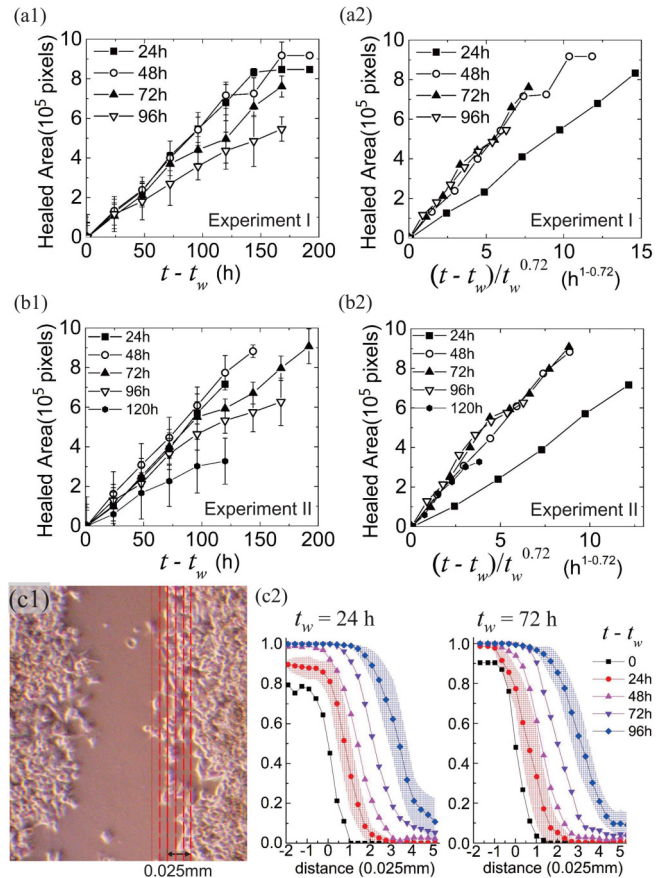

FIG. 4. Closure of wounds in terms of healed areas and density profiles. (a),(b) Healed area as a function of normal and rescaled postwounding time in experiments I and II for different waiting times. The vertical axis is the healed area $A(t_w) - A(t)$, where A is the wound area expressed in 10^5 pixels counted by Photoshop CS6 from the snapshot. Panels (a1) and (b1) show the healing curves on the normal time scale of the postwounding time $t - t_w$, whereas (a2) and (b2) show the data collapse in a renormalized time scale with a rescaling exponent 0.72. Panels (c1) and (c2) show the cell density profiles in experiment I. The vertical axis is the normalized cell density measured as the area covered by the cells divided by the total area in each bin and averaged over all the samples. The shaded areas, red for $t - t_w = 24$ h and blue for $t - t_w = 96$ h, are the error bars drawn with fill area.

profile propagates at a constant speed into the wound bed like a traveling wave, as is extensively documented in previous literature [29–32,37,38]. The shape of the average profile approximates to a sigmoid curve, yet with a wider low-density head at the forefront, especially for $t - t_w > 24$ h. In the comparison between two groups, we find that the profile in group 3 ($t_w = 24$ h) propagates more slowly than that in group 1 ($t_w = 24$ h) with a wider extension in the low-density head. This indicates that the cells at the leading edge can migrate into the denuded area with a normal speed in both groups but the bulk of cells behind in group 3 failed to advance as quickly as in group 1. Moreover, since the profiles in Fig. 4(c2) are bin averaged, we show the standard deviation of the data (the shaded areas, which are the error bars drawn with fill areas) for two postwounding time points in both groups. It

is seen that the error ranges are generally large for all sample sets, with the extended low-density heads at the leading edge having the largest variability for the profiles of $t - t_w = 96$ h in both groups. This is related to the fact that heterogeneity of healing rates across the samples emerges during the profile propagation and peaks at the leading edges: in some samples [for instance, Figs. 3(b) and 3(c), 96 h], several isolated cell clusters or finger-shaped edges formed and promptly invaded into the denuded area ahead of the bulk of the cells (see similar results in Ref. [37]), while in other samples very few of them appeared; the heterogeneous healing rates can also cause a wound closed like a zipper [for instance, Fig. 3(a), 96 h]. A further discussion is presented in Appendix C 3. Nevertheless, no striking difference can be observed in the degree of this heterogeneity between short and long waiting times, hence we do not consider this heterogeneity of healing rates as a viable mechanism for the bio-aging in this study.

3. Summary of experimental observations

From the experimental data, we know several facts: (1) during the waiting time, cell density is slowly approaching a saturation level due to the limit of space and cell viability is exponentially decaying to a nonzero value possibly because of contact inhibition, in which the increase in intercellular adhesion and the accumulation of ECM with time might play important roles; (2) the healing function calculated from the healed area follows a dynamical scaling in relation to the waiting time; (3) the slowdown of healing was not caused by the density growth during waiting; (4) for groups with a larger waiting time, the slowdown of the propagation of the wound edge was mainly caused by the slow advancement of cells behind the leading edge. In the following sections, we construct minimal models based on these facts and detangle the roles of several key factors such as cell proliferation and cell migration to explain the slowdown of healing in experiments. We also identify the control parameter through criticality analysis in the minimal model and later confirm it in a microscopic agent-based model, where the cell-cell and cell-ECM adhesions and the cell cycle process are taken into account.

III. MACROSCOPIC EQUATION-BASED MODEL

One of the simplest macroscopic equation-based models for wound healing without waiting is the reaction-diffusion equation (RDE) proposed by Fisher and Kolmogorov [39,40] and later verified and extended by many others [28–32,37,38,41]. Wound healing models using RDEs attribute the growth of cell density to two factors: cell movement (diffusion) and cell proliferation (reaction). To model the effect of contact inhibition, the diffusivity and growth rate can be formulated as monotonic decreasing functions of cell density [32]. However, traditional RDEs (hereafter referring to the wound healing models using RDEs) can reproduce none of the characteristics of aging observed in the experiments; in fact, the healing events even accelerate with longer waiting times (see Appendix B 1 for an introduction to RDE results). In the following section, we propose a modified RDE model with a minimal set of assumptions to reproduce the aging effects.

A. Asymmetric RDE (ARDE) for wound healing

We first briefly introduce the original RDE model for wound healing. Given a normalized cell density $u(x,t)(0 \leqslant u \leqslant 1)$ at position x in a one-dimensional space at any time t, the time evolution of $u(x,t)$ is

$$\frac{\partial u}{\partial t} = d \frac{\partial}{\partial x} D(u) \frac{\partial u}{\partial x} + mM(u)u, \quad (1)$$

where $D(u)$ and $M(u)$, both decreasing from 1 to 0 as a function of u, represent the normalized cell diffusivity and the normalized cell mitotic rate, respectively. Constants d and m are two coefficients weighting the contributions of the two terms. The formulation of $D(u)$ has many candidates, while we adopt the one proposed by Cai *et al.* [32]:

$$D(u) = \frac{p}{p + u}, \quad (2)$$

where $p > 0$ is a coefficient inversely proportional to the strength of contact inhibition. We set p as 0.01 in the following simulations, hence D can hundredfold decrease from 1 to 0.01 when the cell density u increases from 0 to 1. Conventionally, the proliferation term $M(u)u$ takes the form of logistic growth $(1 - u)u$ [28–32,39–41]. Given the initial condition $u(*,0) = u_0$, the solution to Eq. (1) is a sigmoid function of time for all x, hence the cell density at any t_w immediately before wounding is

$$u(t_w) = \frac{u_0}{u_0 + (1 - u_0)e^{-mt_w}} \quad (3)$$

with the long time limit $u(t_w \to \infty) \approx 1 - u_0/(1 - u_0)e^{-mt_w}$. Therefore, the cell density approaches saturation with an exponentially decaying speed, agreeing with the experimental findings in Fig. 2(a).

When a wound is created, the cell density drops to zero in the wound bed, inducing a dramatic density difference at the wound edge. Then the cells start to diffuse from the high-density region to the low-density region at the speed proportional to $D(u)$ while they proliferate at the rate proportional to $M(u)$. As a result, the cell density profile $u(x,t)$ at the wound edge is a traveling wave, with cells at the low-density region having the highest diffusivity and mitotic rate. The formulation of diffusivity $D(u)$ and mitotic rate $M(u)$ in RDE naturally presumed that the cells can immediately sense the local cell density and response promptly to the wound. Under this assumption, the waiting time elapsed before wounding only slightly affects the cell density at the wounding time [Eq. (3)] without profound impacts on other parts of the dynamics. As is observed from the comparison between experiments I and II (see Sec. II B 2), the density effect cannot be the core reason of aging.

To reproduce the aging effect, a strong dependence of the diffusivity and the mitotic rate on the waiting time is necessary. Therefore, we consider that the cells at the wound edge do not resume their diffusivity or mitotic rate immediately; particularly, the longer the cells wait, the slower the response to the wound should be.

1. Delayed-proliferation model

We first propose a model of delayed recovery in the mitotic rate $M(u(x,t))$ for all x as

follows:

$$M(t) = M_{\text{con}}(t), \quad \text{for } M_{\text{con}}(t) \leqslant M(t - \Delta t)$$
$$M(t) = \delta M_{\text{con}}(t) + (1 - \delta)M(t - \Delta t), \quad \text{for } M_{\text{con}}(t) > M(t - \Delta t)$$

$$(4)$$

where δ ranging from 0 to 1 is a delay fraction, and $M_{\text{con}}(t) = 1 - u(t)$ represents the mitotic rate of the logistic growth, which is subject merely to the contact inhibition. Indeed, Eq. (4) categorizes the dynamics of $M(t)$ into two conditional cases: if $M_{\text{con}}(t)$ is smaller than the mitotic rate at the previous time step $M(t - \Delta t)$, which means that the contact inhibition is getting stronger, then $M(t)$ will be reduced to $M_{\text{con}}(t)$ immediately as the inhibition of mitosis; otherwise if $M_{\text{con}}(t)$ is larger than $M(t - \Delta t)$, which implies a weaker contact inhibition at the current time, $M(t)$ would recover to $M_{\text{con}}(t)$ at a delayed pace controlled by the fraction δ. Apparently, the increase and decrease in $M(t)$ depends asymmetrically on $M_{\text{con}}(t)$, hence asymmetrically on $u(t)$. In the extreme case of $\delta = 0$, $M(t)$ will decrease everlastingly, thereby modeling an irrevocable cell cycle inhibition. Contrastingly, in the case of $\delta = 1$, the recovery of mitotic ability becomes instantaneous, and Eq. (4) will return to the logistic growth form. For a clearer biological interpretation, δ characterizes how rapidly cells can wake up from an arrest state (the state of cell cycle arrest). For $0 < \delta < 1$, the transition from a growth state to an arrest state will be faster than its reversal process for a cell. For such a loss of symmetry in the transitions between two cell states, the term asymmetric RDE (ARDE) is used to name our model.

The numerical solutions to the ARDE model with a delay in the proliferation term for different delay fractions and waiting times are exhibited in Fig. 5. The wound condition is set as $u(x^{\text{wound}}, t_w) = 0, x^{\text{wound}} \in [x', x'']$. Figures 5(a1) and 5(a2) show that the density profile $u(x, t)$ still keeps the form of a traveling wave, although the exact front shape and the propagation speed depend on the delay fraction δ. A small value of δ can slow down the wave propagation as well as the transient formation of the stable front shape; meanwhile, the low-density head of the cell front extends much wider with a small δ [Fig. 5(a1)] than that with a large δ [Fig. 5(a2)]. Figure 5(b) shows the comparison of the density profiles between two different waiting times with the same value of δ. Similarly, the larger waiting time causes a slowdown of front formation and propagation, with the stable wave shape of the fronts having the extended head in the low-density region. The slowdown of the front propagation and the change in the front shape due to the small δ or the long waiting time suggest that the delayed recovery of cell proliferation can slow down the advancement of the bulk of cells behind the leading edge, agreeing well with the experimental results [Fig. 4(c2)].

The healed area as a function of postwounding time is displayed in the top panel of Fig. 6 with three different values of δ [Figs. 6(a1)–6(a3)]. In the figures, the vertical axis of graph is the normalized healed area calculated as

$$\tilde{A}(t) = \frac{1}{|x'' - x'|} \int_{x'}^{x''} u(x, t) dx.$$

The loss of healing ability of cells with a longer waiting time is clearly demonstrated by the slower increase in $\tilde{A}(t)$.

In the lower panels of Figs. 6(a1)–6(a3), the healing data with longer waiting times ($t_w > 36$ steps) could be rescaled to a single curve with distinct scaling exponents for three different δ, whereas the healing curves with shorter waiting times ($t_w = 12, 24$ steps) deviate from the dynamical scaling, just as the healing of group 1 did in the experiments. The decrease in δ (from 10^{-5} to 10^{-7} and 10^{-9}) induced an increase in the scaling exponent (roughly from 0.48 to 2.33 and 4.35), revealing the role of δ in controlling the deterioration of healing efficiency.
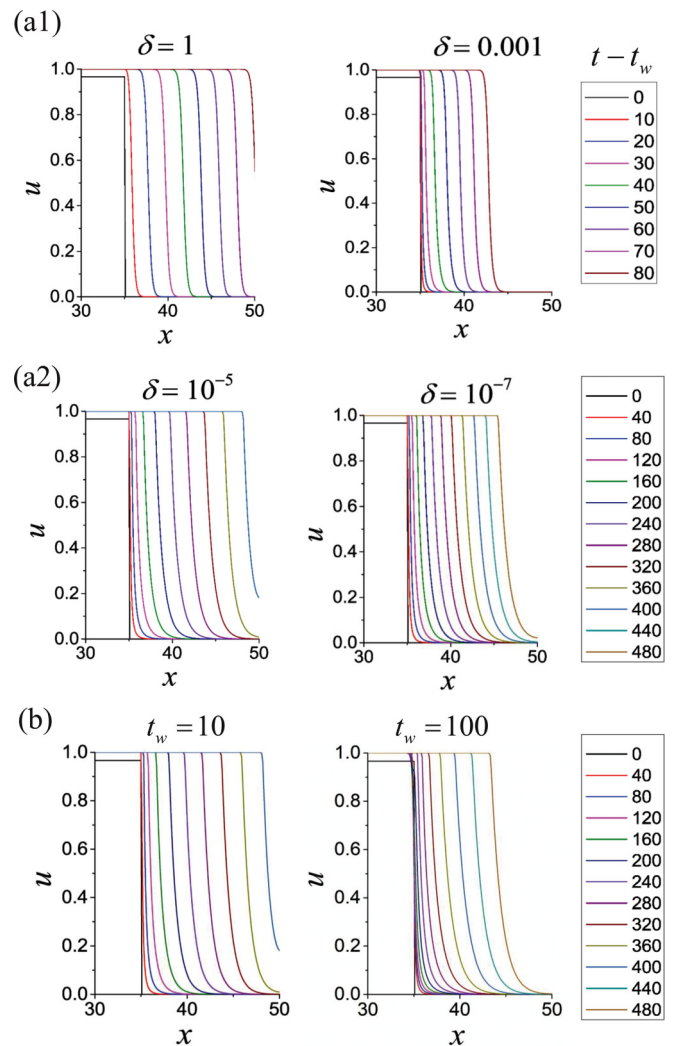

FIG. 5. Numerical results of the postwounding cell front propagation in asymmetric reaction-diffusion equation (ARDE) model with a delay in the proliferation term solved with $u_0 = 0.9$, and $d = m = 0.1$, $p = 0.01$ on $x \in [0, 100]$: (a1) and (a2) for different values of delay fraction δ with $t_w = 10$ and (b) for different waiting times t_w with $\delta = 10^{-5}$. The total wound area ranges from $x = 35$ to $x = 65$. Only the left side of the wound edge is shown because the density profiles on two sides are mirror symmetric.
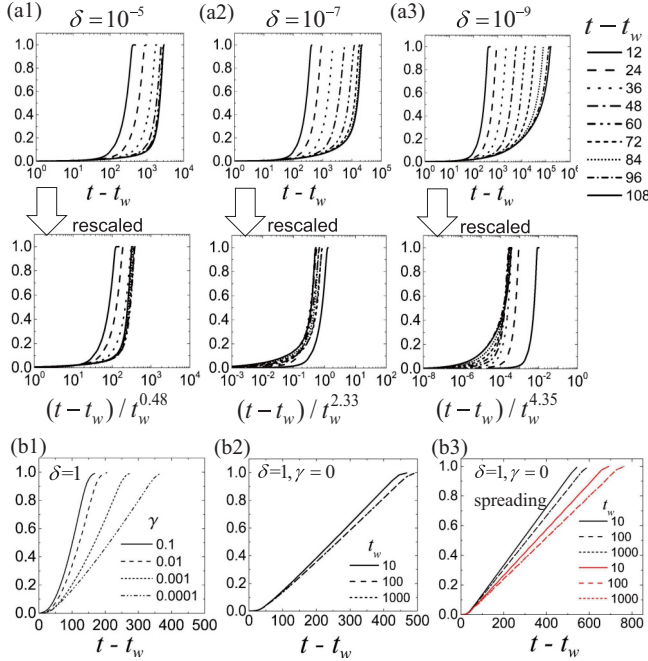
FIG. 6. Numerical results of the normalized healed area as a function of postwounding time in asymmetric reaction-diffusion equation (ARDE) model with $d = m = 0.1, u_0 = 0.5, p = 0.01$. The vertical axes represent the normalized healed area $\tilde{A}$. (a1)–(a3) For three values of the delay fraction δ in the proliferation term. The aging exponent increases when δ decreases and results of the first two groups $t_w = 12$ and $t_w = 24$ deviate from the rescaled curve. (b1) For different values of the delay fraction γ in the diffusion term with $t_w = 0$. (b2) For different values of waiting times. (b3) For different values of waiting times with the modeling of spreading cells. The black curves refer to $\lambda = 0.001$; the red curves refer to $\lambda = 0.01$, where λ controls the length of the region occupied by the spreading cells. Note that the x axes in panels (a1)–(a3) are on logarithmic scales.

The reason a small δ can render a huge aging exponent may be inferred from the following asymptotic analysis of mitosis rate M. Assuming that all cells in the wound area experience delayed recoveries of mitotic rate and that the cell diffusion is negligible, we can derive the following time evolution equation for the mitotic rate from Eq. (4):

$$M(t,t_w) = \int_{t_w}^{t} \delta(1-\delta)^{t-t'}[1-u(t')]dt'$$
$$+ (1-\delta)^{t-t_w}[1-u(t_w)]. \quad (5)$$

Equation (5) consists of two terms: a convolution from t_w to t and a contribution from the density $u(t_w)$ immediately before wounding. Apparently, a small δ will reduce the contribution of the convolution term, and in the extreme situation $\delta = 0$, $M(t,t_w)$ is reduced to $1 - u(t_w)$, which approaches e^{-mt_w} in the limit of $t_w \to \infty$. The exponential decay in the mitotic rate M with t_w implies an exponential divergence of healing time with t_w, which leads to an infinite aging exponent for the dynamical scaling [also demonstrated by Fig. 7(b), and see the discussions in Sec. III B].
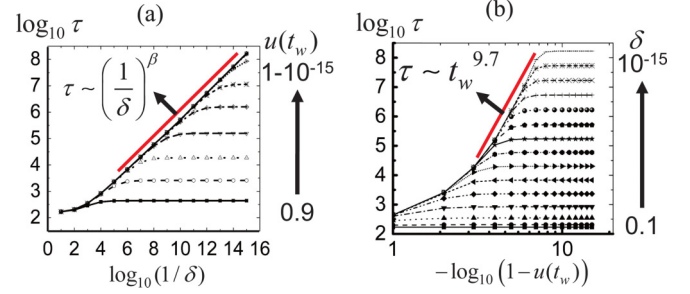

FIG. 7. Critical behaviors in asymmetric reaction-diffusion equation (ARDE): complete healing time τ diverges as a function of delay fraction δ, and cell density at wounding time $u(t_w)$. (a) $\log_{10}\tau$ vs $\log_{10}(1/\delta)$. The lines from the bottom to top correspond to $u(t_w) = 1 - \epsilon, \epsilon$ from 10^{-1} to 10^{-15}. (b) $\log_{10}\tau$ vs $\log_{10}[1 - u(t_w)]$. Note that $\log_{10}[1 - u(t_w)]$ is asymptotically proportional to t_w according to Eq. (3) and the horizontal axis is on a logarithmic scale. The curves from the bottom to top correspond to δ from 10^{-1} to 10^{-15}.

2. Delayed-migration model

Cell migration can also be suppressed by the increased cell density or the accumulation of cell-cell or cell-ECM adhesion [28–33,37,38]. Previous literature reveals that the motility of the cells will change over time in a confluent cell sheet [22,23] and the mechanics related to migratory ability of the cells at the wound edge influence the wound closure efficiency [36,42–45]. In a similar way to Eq. (4), we can realize the impact of the waiting time on the cell migration by adding the "wake-up" dynamics to the diffusion term in Eq. (2) as follows:

$$D(t) = D_{\text{con}}(t) \quad \text{for } D_{\text{con}}(t) \leqslant D(t - \Delta t)$$
$$D(t) = \gamma D_{\text{con}}(t) + (1-\gamma)D(t) \quad \text{for } D_{\text{con}}(t) > D(t - \Delta t)$$
$$, \quad (6)$$

where γ from 0 to 1 is the delay fraction for the diffusivity. Figure 6(b1) shows that, with a smaller γ, the wound heals more slowly for $t_w = 0$. Nonetheless, even if we fix γ to zero (which means an irreversible decrease in the cell motility due to the maturation of the inter- and extracellular conditions), no notable aging effect is observed [Fig. 6(b2)].

This result is unexpected from the previous literature in which the emergence of nonproliferative spreading cells at the leading edge (around which lamellipodia can be found; see Appendix E) and their motility were reported to be crucial for healing efficiency. In ARDEs, such spreading cells are not modeled. To test whether this absence of spreading cells can explain the loss of the aging effect, we add the submodel of spreading cells by multiplying a Heaviside step function $H[\lambda - D(x)]$ to the original mitotic rate obtained from Eq. (4). Hence, when the cells have a diffusivity D larger than λ, they will have zero mitotic activity. The newly introduced parameter $\lambda > 0$ controls the length of the region occupied by the spreading cells. Since these cells only appear in the front rows of the wound edge [28,36,42–45], λ should be small compared with the diffusivity coefficient d (refer to Appendix E). Figure 6(b3) shows the healing curves for $\lambda = 0.001$ (black) and $\lambda = 0.01$ (red) in the case of $\delta = 1, \gamma = 0$ under various waiting times. By comparing Figs. 6(b2) and 6(b3), we find that when λ is small, the role of spreading cells

is negligible. The healing processes apparently appear slower with a larger λ, yet still no notable aging effect is observed.

If we further consider reproducing the extended heads in the density profiles as is shown in the experiment, we should apply the wake-up dynamics [Eq. (6)] only to the bulk of cells behind the leading edge, which will make the unnoticeable aging effect in Fig. 6(b) even more trivial (results not shown here).

In brief, the wake-up dynamics for the diffusion term in ARDE do not render slowdown of healing unlike its counterpart for the proliferation term. This can be attributed to the fact that the diffusivity D does not decrease radically with large waiting times [because the diffusivity D takes the form of $p/(p + u)$; in fact, any monotonic decreasing function of u satisfying $D(u = 1) > 0$ cannot reproduce aging]. To induce an aging effect by modifying the diffusion term in the RDE models, we must add extra assumptions, such that the diffusivity coefficient d decreases or the range of spreading cells λ increases radically with the waiting time in a specific fashion. However, the evidence is still lacking. Though the inhibition of cell locomotion due to the densification of the confluent cell sheets in short-time observation has been reported [16,18,22], cell proliferation and the remodeling of ECM were not triggered in these experiments. For healing processes longer than the cell doubling time (which is the estimated duration for a cell to divide and roughly 24 h for HepG2.2.15 cells in our experiments), whether the diffusivity decreases or the range of spreading cells increases with longer waiting times and whether the cell migration can be resumed promptly remain to be investigated in future experiments.

3. Summary of ARDE modeling for wound healing

The delayed recovery of cell proliferation in ARDE models can well reproduce the dynamical scaling of the waiting-time-dependent healing events (including the late onset of aging) and the slow propagation of the cell fronts with an extended low-density edge. Contrastingly, the delayed migration model cannot induce the aging phenomenon without extra assumptions on the evolution of other parameters. Nevertheless, considering that the cell motility and cell cycle dynamics are coordinately regulated by a complex signaling network of intracellular molecules, we are aware that the slowdown of healing is a combined consequence of the mechanical and biochemical factors. More experimental efforts should help unveil the detailed mechanisms underlying this slowdown of healing and identify the specified roles of cell proliferation and cell migration.

B. Bounded criticality

A scaling between delay fraction δ and complete healing time τ is also revealed by numerical simulations, where τ is defined as the time when the normalized healed area $\tilde{A}(t) > 99\%$. Figure 7(a) illustrates the divergence of τ with δ under various $u(t_w)$. A larger value of $u(t_w)$ corresponds to stronger contact inhibition due to a longer waiting time, as shown in Eq. (3). The algebraic divergence of τ as $\tau \sim (1/\delta)^\beta$ ($\beta = 0.47$ is universal for all parameters; see Appendix B 2) resembles the criticality in physical systems with the critical point at $\delta = 0$, even though the divergence crosses over to a ceiling for a small

δ. A larger wounding density $u(t_w)$ postpones this crossover, suggesting that δ serves as a control parameter similar to a physical control parameter (e.g., temperature) under the condition of stronger growth inhibition (caused by higher cell density). The reason for the ceiling in the small δ region is that as δ decreases, the second term involving $u(t_w)$ becomes more dominant in $M(t,t_w)$ [see Eq. (5)], and thus τ diverges as $\tau \sim e^{mt_w}$ independently of δ. Under stronger contact inhibition [with $u(t_w)$ closer to saturation], the convolution term in Eq. (5) can take effect with a smaller δ, and thus extend the range of critical regime.

Figure 7(b) shows the relationship between $\log_{10} \tau$ and $\log_{10}[1 - u(t_w)]^{-1}$ for a series of δ, noting that $\log_{10}[1 - u(t_w)]^{-1}$ is asymptotically proportional to t_w according to Eq. (3). The aging regime, in which τ increases with t_w, also crosses over to a ceiling; a smaller δ renders a rapid divergence of τ (indicative of a dramatic aging) with an extremely large aging exponent ($\tau \sim t_w^{9.7}$, the red line). Additionally, the aging regime begins with an exponential subregime and then crosses over to a power-law one, which is more explicit with a smaller δ. This shift of subregime elucidates why groups with a shorter wait failed to fit dynamical scaling in ARDE results [see Figs. 6(a1-a3)]. Finally, the vanishing of the aging effect at extremely long waiting times originates from the existence of cell diffusion as demonstrated in Appendix B 3.

IV. SLOWDOWN OF HEALING IN AN AGENT-BASED MODEL

To justify the biological contents of the delay fraction δ, we further explored the aging phenomena *in silico* using a cell-based approach that involves more detailed cell behaviors than the ARDE models do.

A. Simulation results with discrete receptor dynamics model (DRDM)

We adopted DRDM, an on-grid agent-based model for epithelial tissue formation [46]. DRDM can reproduce diverse tissue homeostatic states, including degenerate, normal, and tumorigenic states merely based on cell-cell and cell-ECM interactions without predefined mutations or environmental changes. In the DRDM simulation, each cell secretes ECM during growth and adheres to its ECM and neighboring cells; when the cell-cell and cell-ECM adhesions are both strong enough, the cell becomes polarized and prepared for cell cycle arrest; cells can diffuse only if the cell-cell and cell-ECM adhesions are weak. The cells in DRDM are equipped with five types of receptors, the expressions of which discretely change in response to the cell behavior in the previous time step and then dictate the cell behavior for the next discrete time step based upon comparisons between the receptor amounts and respective thresholds (refer to Appendix C for a detailed description). The primary finding from the DRDM in the previous study [46] is that healthy tissues intrinsically evolve into tumorigenic states (which feature large tissue volumes with mostly proliferating cells) accompanying a decrease in average cell age or else into degenerate states (which feature diminished tissue volumes with mostly quiescent cells)
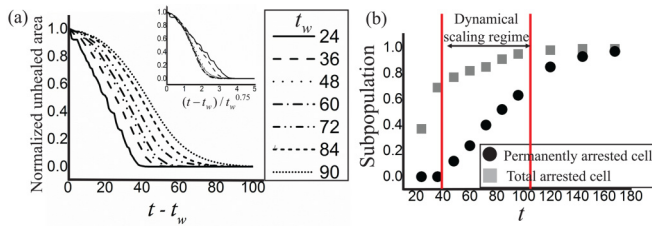
FIG. 8. The slowdown of healing in the simulations with discrete receptor dynamics modeling (DRDM) using the degeneration-inducing parameters. (a) Healing processes on a normal and a rescaled time axis (inset). Note that groups with waiting time t_w larger than 36 steps obey the dynamical scaling with an aging exponent 0.75. (b) Time evolution of population densities for arrested cell during natural growth before wounding. Arrest cells are cells with arrest receptor amount above arrest threshold a. Permanently arrested cells are defined as the arrested cells with the sum of growth and adhesion receptor amount below growth threshold g.

accompanying an increase in average cell age over a large spectrum of time scales. We thus used the parameter settings that reproduced normal-to-degenerate evolution accompanying aging in our simulations (model details and the snapshots of simulated healing events are displayed in Appendix C 1 and Appendix C 2).

As expected, the healing process decelerated with waiting times t_w [Fig. 8(a)], and for t_w from 36 to 90 iterations, the healing curves fit dynamical scaling with an exponent of 0.75 [inset of Fig. 8(a)]. Scrutinizing the dynamics of the subpopulations during the natural growth before wounding, we observed a growing population of cell-cycle arrested cells undergoing three regimes [Fig. 8(b)], the second of which (with a steady linearity) is concomitant with the dynamical scaling regime. This suggests that the critical factors relating to delay fraction δ can be those driving the structural shift in the cell subpopulation.

B. Criticality of multiple factors

The dynamics of the subpopulation structure in DRDM are affected by multiple factors, including cell-ECM adhesion, cell-cell adhesion, cell polarization, the regulation of cell-cycle arrest, apoptosis, and cell movement. Because apoptosis is negligible in the *in vitro* cell monolayer formation, only the effects of the ECM threshold e, polarization threshold p, arrest threshold a, and growth threshold g are examined.

We first explain how these four thresholds function in DRDM. Growth threshold g: the number of growth receptors exceeding the growth threshold is a prerequisite for cell growth. ECM threshold e: the number of ECM receptors (or the receptors bound to ECM) exceeding the ECM threshold is one of the prerequisites for a cell to be polarized into an apical state; the ECM threshold thus inversely correlates with the sensitivity of a cell to ECM. Polarization threshold p: the number of adhesion receptors exceeding the polarization threshold is the other prerequisite for a cell to polarize. Arrest threshold a: arrest receptors begin to accumulate once a cell becomes polarized, and if the number of arrest receptors hits the threshold a, the cell cycle will be arrested into a state with

no more growth and with weakened adhesion to other cells and the ECM, i.e., a state referred to as cell cycle arrest.

Healing time $\tilde{\tau}$ in the DRDM simulation is defined as the time when 90% of the wound sites are reoccupied by cells, and is measured for different sets of e, g, a, and p. As a result, e and g are the two most critical factors that slow the healing as illustrated in Fig. 9(a); in contrast, p and a play insignificant roles in aging [Fig. 9(b)]. However, the abrupt jump of $\tilde{\tau}$ from roughly 50 to infinity in Fig. 9(b) corresponds to the emergence of incomplete healing, which is another complex issue that has not been evaluated in experiments or ARDE models; we give explanations on incomplete healing in Appendix C 3.

The dependence of healing efficiency on the ECM threshold e [Fig. 9(c2)] shows that the ECM plays a role in the slowdown of healing. A lower value of e induces a quicker polarization that may lead to cell cycle arrest, suggesting that the accumulation of ECM induces the slowdown of healing in DRDM through promoting cell cycle arrest. The growth of ECM in DRDM can meanwhile affect the cell motility. Nevertheless, as we have shown in Appendix C 4, the loss of cell mobility cannot lead to a significant aging effect in DRDM, in agreement with the correspondent findings in the ARDE models. Hence, the aging effect associated with ECM in DRDM simulations is caused by cell cycle arrest instead of the mechanical reasons.

Healing times diverge continuously with g as a power law $\tilde{\tau} \sim g^{\tilde{\beta}}$ for small g [Fig. 9(c1)]. Clearly, $1/g$ serves as a control parameter as the delay fraction δ does in ARDE [see Fig. 7(a)] and the criticality vanishes for both smaller $1/g$ and δ. However, the slope of $\log_{10} \tilde{\tau}$ vs $\log_{10} g$ (i.e., the value of critical exponent $\tilde{\beta}$) differs with other parameters such as various ECM thresholds e [Fig. 9(c2)] and various arrest thresholds a [Fig. 9(d)], indicating that g is not as dominant as δ for controlling the dynamical scaling.

Nonetheless, the essence of δ can still be understood by associating δ with g. In DRDM, growth threshold g determines the asymmetry of the regulation in the restriction point (a checkpoint for entry and exit of cell cycle arrest): entry into arrest depends only on the arrest receptors, whereas the exit from arrest requires additionally the growth receptor amount exceeding g [Fig. 10(a)]. When g is zero, entry into and exit from cell cycle arrest are governed solely by arrest receptors, i.e., the transitions between growth and arrest become symmetric. Otherwise for any nonzero g, quiescent cells must have their growth receptor amount overcome an extra barrier of g. If g is too large, cells can rarely restore the growth, and the growth-to-arrest transitions in the cell states are irrevocable. The arrest-to-growth (or the growth-to-arrest transition) in DRDM cells is exactly a microscopic representation of the increase (or decrease) in the mitotic rate M in the ARDE [Eq. (4)], and the growth threshold g in DRDM, similar to that of δ in the ARDE model [Fig. 10(b)], controls the deterioration of healing efficiency [referring to the inset of Fig. 9(a)]. In addition, just as the critical role of δ is more prominent under stronger contact inhibition in ARDEs [Fig. 7(a)], and the criticality or aging in DRDM controlled by g is likewise more apparent under growth-inhibitive settings such as a low ECM threshold [Fig. 9(c1)], a low polarization threshold (a sensitive polarizing response to cell-cell adhesion), or a low arrest threshold [a strong cell-arrest regulation; see Fig. 9(d)].
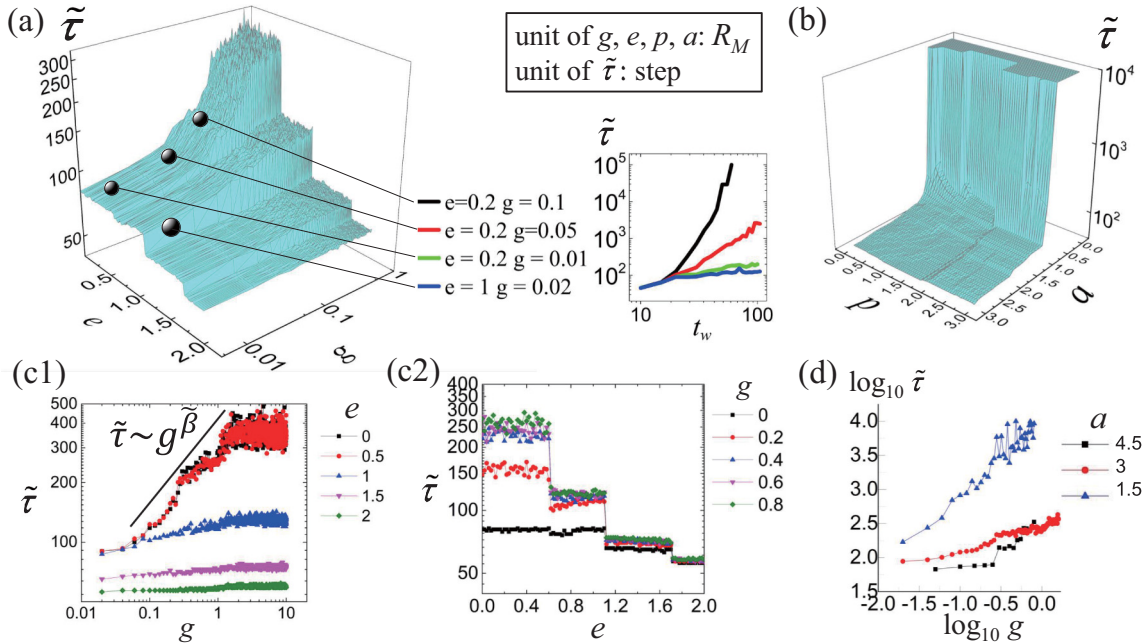
FIG. 9. Healing time $\tilde{\tau}$ in discrete receptor dynamics modeling (DRDM) with different parameter settings. All wounds are set to be performed at ten steps after the start of the simulation. The values of thresholds e,g,p,a on the figures are in the unit of R_M, which is the receptor amount required for mitosis. See Appendix C for other parameters. (a) Healing time $\tilde{\tau}$ vs extracellular matrix (ECM) threshold e and growth threshold g. Inset: the log-log plot of $\tilde{\tau}$ vs t_w with four pairs of $\{e,g\}$ pointing to the black balls on the 3D diagram. (b) The diagram in the space of polarization threshold p and arrest threshold a, with e fixed at $0.8R_M$ and g at $0.05R_M$. The infinitely diverged values of $\tilde{\tau}$ are truncated to 10^4. (c) The 2D log-log plot of $\tilde{\tau}$ vs g and the log-linear plot of $\tilde{\tau}$ vs e. (d) The divergence of $\tilde{\tau}$ as a function of g for different arrest thresholds a, with $e = 0.8R_M$.

Given the fact that the delay fraction δ has been substantiated by the growth threshold g in many aspects, we can interpret the critical parameter for bio-aging in the wound healing context as the degree of asymmetry between growth-to-arrest and arrest-to-growth transitions in cell cycle governed by the restriction point. This asymmetry is hereafter briefly termed as *restriction asymmetry*.

V. DISCUSSION

A. A comparison of physical aging and bio-aging

1. Analogy in the picture of trap model

Over the past decade, the analogy between glassy or jammed materials and cellular layers has been studied on
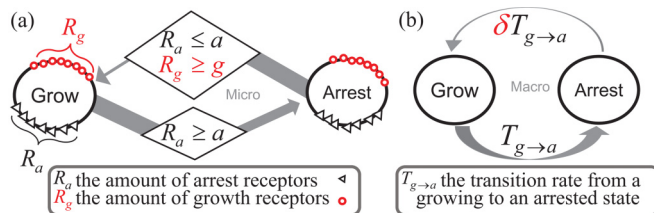

FIG. 10. Asymmetric transitions between cell growth and cell cycle arrest in discrete receptor dynamics modeling (DRDM) as a microscopic interpretation (a) and in asymmetric reaction-diffusion equation (ARDE) as a macroscopic interpretation (b). The thickness of the arrows represents the transition rate.

the basis of mechanobiology. Many mechanistic features of cytoskeletal dynamics were found, such as dynamic heterogeneity, cooperativity, and kinetic arrest, and these glasslike mechanics are speculated to have a profound impact on the biochemical activities of the cellular layers [16–19]. Although the interdependency and causality between the glasslike mechanics and the slowdown of healing are not fully clarified, we are able to establish an analogy between the slowdown of healing in the cell monolayer and the slowdown of relaxation in physical systems based on the current findings in experiments and simulations.

The analogy between the two types of aging can be articulated with the *trap* model [47]. In a system with many particles (or cells), each particle (or cell) senses a local energy trap (or a biochemical trap that induces cell cycle arrest) formed by neighbors (or ECM, cell-cell adhesion); the escape from it requires more effort than does entering into it. When the control parameter approaches a critical value, the barrier of the traps will become so high that the system dynamics may easily be captured in the local minimum of the total free energy. In this analogy, the two systems based on disparate dynamics resemble each other, having a common definition of the control parameters as the ratio of the effort required to fall into a trap (arrest) to the effort required to escape. Typically, when this ratio is small (e.g., low temperature, high density in physical systems and small δ in ARDE), the dynamics of the particles (or cell cycles) tend to be arrested and the system loses the ability to relax in physical systems (or to regenerate in biological systems).

2. Unclarified issues

Due to the low time resolution and the short observation time scale of the current experiments of TDWHAs, a finer comparison between the slowdown of healing and the slowdown of relaxation events in physical systems is limited, thus leaving many unclarified issues associated with the analogy between two types of aging. For instance, dynamical scaling of physical aging is believed to originate from time-spatial local scale invariance symmetry [48], a property that currently has no biological counterpart. Also, the scaling exponent of physical aging typically ranges from 0 to 1, whereas in the proposed ARDE, this exponent can be far greater than 1 when δ is close to zero; this suggests a possibility that the exact scaling of the healing curves in relation to the waiting time might be exponential, instead of a power law. Meanwhile, the critical range of the control parameter found in the biological model is restricted and influenced by many other factors such as cell movement, cell-ECM interactions, and cell polarization, among others, implying that the living systems with tremendous complexity might be no perfect analog of any physical systems. Finally, the concepts of equilibrium and relaxation in physics (associated with ergodicity and a process of reaching ergodicity) do not rigorously correspond to tissue homeostasis and regeneration (where only nonergodic steady states are possible) and it is unclear to what extent this fundamental discrepancy could falsify the analogy and impair its application prospects. These issues may provide many new research themes for future studies.

B. Implications for modulating regeneration

1. Reducing restriction asymmetry

In the model analyses, the key factors in bio-aging were identified as (1) *growth inhibition* (resulting from cell-cell contact and cell-ECM interactions, among others), which is the prerequisite, and (2) *restriction asymmetry*, the controller for the "wake-up" dynamics from the deep *growth inhibition*. For better regeneration, reducing the inhibition of cell growth is risky because growth inhibition is naturally programmed for tissue stability and tumor suppression. Nevertheless, reducing the asymmetry of cell-cycle regulation can enhance regeneration without risking tumorigenesis assuming natural growth inhibition is undisturbed. Therefore, administrating *restriction asymmetry* in the clutter of biological details is crucial.

Restriction asymmetry in tissue may result from irreversibility of the activation route of signaling pathways [49,50] or can emerge from the monotonic shift of cell subpopulation structure [6]. Practical application to the regeneration of a specific tissue such as the liver tissue requires a full understanding of *restriction asymmetry* in a computational model exclusive to the hepatocytes in a multicellular context before key factors can be tuned in relevant experiments. However, we should always be aware that the delayed wake-up of cell activity may only be one possible ingredient attributed to tissue aging. In some circumstances, other factors such as the deterioration of the environment or the age-dependent pathogenesis can play more prominent roles.
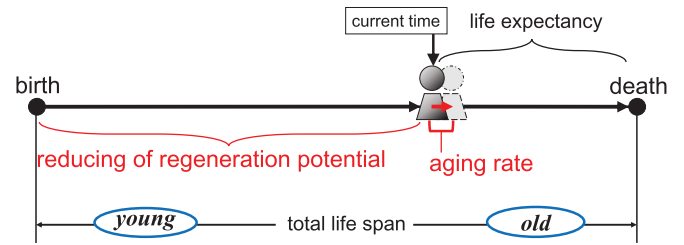

FIG. 11. Measuring aging in a system's life excursion. Traditional biomarkers are focused on life expectancy (i.e., the chronological distance from the present to death); whereas, the dynamical scaling exponent μ in this article quantitatively describes regeneration-related aging rate from young to old.

2. Evaluating regeneration-related aging rate

Measurements of aging are difficult because of the complexity of the interactions among contributing factors [51]. Numerous studies have revealed the genetic determinants of longevity [52] and placed a focus on life expectancy, i.e., the chronic distance to life termination (death; Fig. 11). However, the distance from the beginning of life (birth) and the speed of aging should also provide much information about the regenerative potential, which would facilitate health maintenance. The dynamical scaling exponent μ obtained by fitting the wait-dependent healing processes in our study can serve as a quantitative description of the regeneration-related aging rate of a tissue on its life excursion from young to old age. Even though our protocol for measuring μ is inconvenient for *in vivo* experiments, μ can be easily measured *in vitro* for any cell lines of interest with any specific environment settings.

VI. SUMMARY

Dynamical scaling of multicellular regeneration in time-delayed wound healing assays (TDWHAs) reveals an otherwise invisible link bridging physical and biological aging. The scaling provides an exponent that indicates the regeneration-related aging rate and also sheds light on a methodology for pinpointing the controller of the biological organizations in maintaining the capacity for regeneration. Under the mapping of multicellular regeneration to physical relaxation, parallel models at the macro- and microscopic levels have identified *restriction asymmetry* of cell-cycle processes (the asymmetry of the transitions between the growing and the arrested states) as the most viable role in reproducing the dynamical scaling of healing events. *Restriction asymmetry* serves as a biological control parameter analogous to the control parameters found in physical systems: it controls the speed of slowdown of healing (relaxation) and the power-law divergence of the healing time (relaxation time) near the critical point; yet, its critical role in controlling aging is more prominent under strong growth inhibition caused by specific cellular mechanisms, such as strong cell-cell and cell-ECM interactions. The unification of two seemingly incomparable types of aging in this study not only facilitates an integrated understanding of the bio-aging mechanism but also suggests the further applicability of nonequilibrium physics to complicated life phenomena beyond thermal and mechanical levels. We expect future studies of
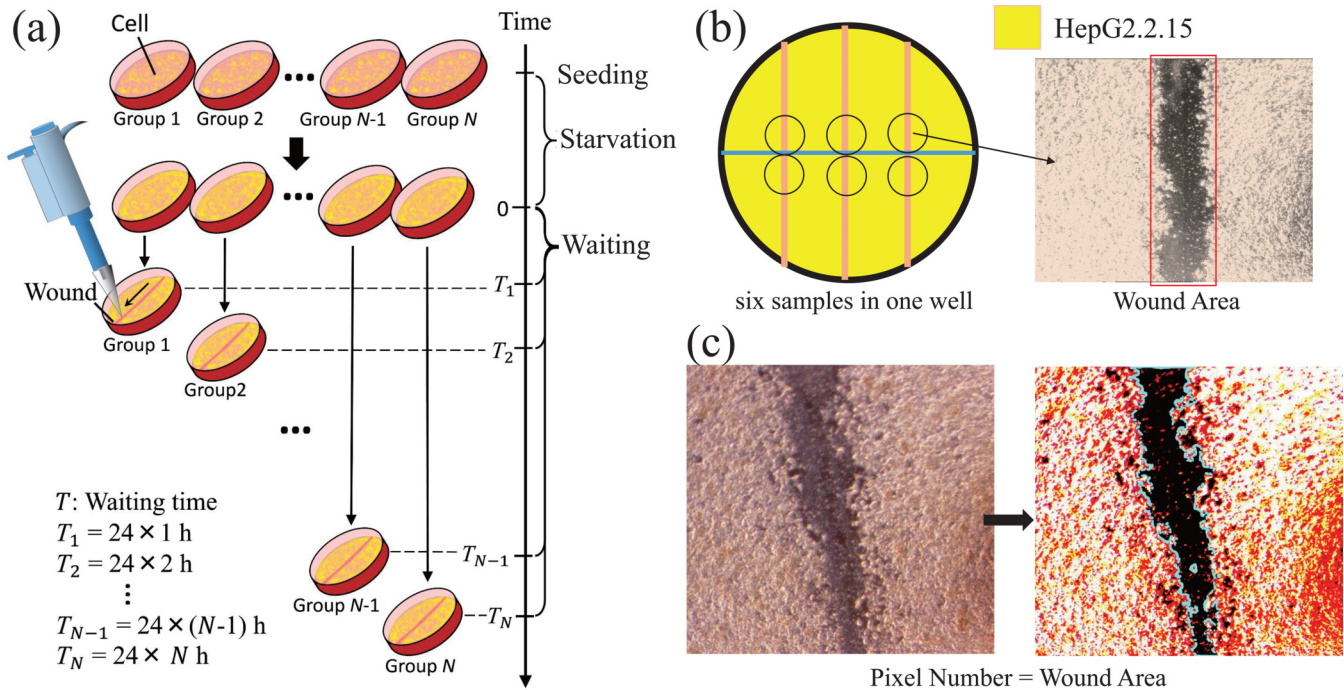
FIG. 12. Time-delayed wound healing assays. (a) The procedures in time sequence: Seeding, starvation, waiting and wounding. Group number N corresponds to a waiting time of $24 \times N$ h. (b) Left: one well has three scratches (wound gaps), as represented by the vertical pink lines; six sample areas, marked by six circles, were located in the center, adjacent to the horizontal auxiliary blue line, which was manually drawn to help locate sample positions. Right: the photograph for each sample taken by a microscope (magnification: 400 ×), where the dark area is the wound area. (c) Postprocessing of images using Photoshop CS6. First, we tuned up the contrast and exposure rate of the snapshot, and then use the Magic Wand for an accurate identification of the wound area. The number of pixels enclosed by the wound edges (the highlighted cyan curves) was calculated automatically by the software.

TDWHAs to involve various cell lines and experimental settings at higher time resolution and with longer waiting periods for clarifying the detailed mechanism underlying the slowdown of healing and for better translating the theory of physical aging to bio-aging problems.

APPENDIX A: MATERIAL AND METHODS

1. Cell line and cell culture

HepG2.2.15 hepatocellular carcinoma cells were maintained in high-glucose Dulbecco's minimal essential medium (DMEM; Gibco, ThermoFisher Scientific), supplemented with 10% fetal bovine serum (US origin, Gibco, ThermoFisher Scientific) at 37 °C and 5% CO_2. The medium was changed twice a day to ensure sufficient nutrients for the cells throughout the entire experiment.

2. Cell counting with a hemocytometer

Cell suspension (10 μL) was taken using a pipette and the pipette tip was placed near the edge of the chamber, allowing the cell suspension to enter the counting chamber by capillary action. The microscope was then focused on an area of the counting chamber and the cells were counted using a tally counter. The average cell count was taken from each of the sets of 16 corner squares and multiplied by 10 000-fold. The final value was the number of viable cells per mL in the original cell suspension. The total cell number in a well was then calculated as this density value times the volume of the total cell suspension in a well (10 mL).

3. Cell viability with 3-(4, 5-dimethylthiazol-2-yl)-2, 5-diphenyltetrazolium bromide (MTT) assays

The medium was removed from each sample of the well and replaced with fresh culture medium. Then MTT (5 mg/mL) was added to each well to a final concentration of 10%. The cells were incubated at 37 °C for 4 h. SDS-HCL solution (10% SDS in 0.01 M HCL) was then added to each well and mixed thoroughly using a pipette tip. Cells were then incubated at 37 °C for another 4 h in a humidified chamber. Finally, the samples were mixed and absorbance was read with a spectrophotometer at 550 nm (reference 750 nm), indicating the metabolic viability of the total cells in the well.

4. Procedures

Newly thawed HepG2.2.15 cells were passaged at confluence, and seeded into six-well plates at an initial density u_0, followed by a period of cell starvation for synchronizing cell cycles. At the end of starvation, the time was reset to zero. As illustrated in Fig. 12(a), the plates of cells were divided into N groups, each of which awaited an additional

TABLE I. Parameter settings for two separate experiments of time-delayed wound healing assays.

Item	Description/value
Pipette type	Gilson, 200 μL/tips (200 μL)
Average wound bed width	0.25 mm
Starvation time before waiting	24 h
Initial seeding cell density	5×10^5 (experiment I),
(per mL)	2×10^6 (experiment II)
Group number	4 (experiment I), 5 (experiment II)

period of time $T_N = 24 \times N$ (h) before subjected to wounding (using a pipette). For each well in the plates [the left graph of Fig. 12(b)], three linear parallel wound gaps were created (the vertical pink lines), with six samples located at the center of the well [the six circled areas adjacent to the horizontal auxiliary blue line in Fig. 12(b)]. Each group was under continuous observation for ~190 h and photographed once every 24 h. The right panel in Fig. 12(b) presents a typical snapshot from the experiments. The photographs were postprocessed in Adobe Photoshop CS6 for counting the pixel number in the wound areas using the Magic Wand Tool [Fig. 12(c)]. Two series of experiments were conducted with two different sets of initial density u_0 and group number N. See Table I for a summary of parameter settings in the experiments.

APPENDIX B: WOUND HEALING BY REACTION-DIFFUSION EQUATION (RDE)

1. Models failing to reproduce slowdown of healing

Let us consider the following RDE:

$$\frac{\partial u}{\partial t} = \frac{\partial}{\partial x} D(u) \frac{\partial}{\partial x} u + M(u)u, \quad \text{with}$$

$$D(u) = p/(p+u), \quad \text{and} \quad M(u) = 1 - u^q.$$

Coefficients p and q determine the strength of the dependence of the normalized diffusivity D and the mitotic rate M on the cell density u, respectively. Note that $q = 1$ yields the Fisher model evaluated in the main text. Spatial coordinates range as $x \in [0,100]$ with a wound condition initialized at different waiting times, $u(x^{\text{wound}}, t_w) = 0, x^{\text{wound}} \in [35,65]$.

The numerical solutions of RDEs with different sets of $\{p,q\}$ are illustrated in Fig. 13(a). Contrary to what we observed in experiments, there is an acceleration of healing with waiting time. This is because a longer waiting time can cause more cells to accumulate at the wound edge before healing starts, which later results in more migration of cells into the wound area and consequently a faster rate of healing [i.e., the red line advances more quickly than the black line in Fig. 13(b)]. Therefore, the original reaction-diffusion model that involved only contact inhibition was not able to reproduce the phenomena of aging.
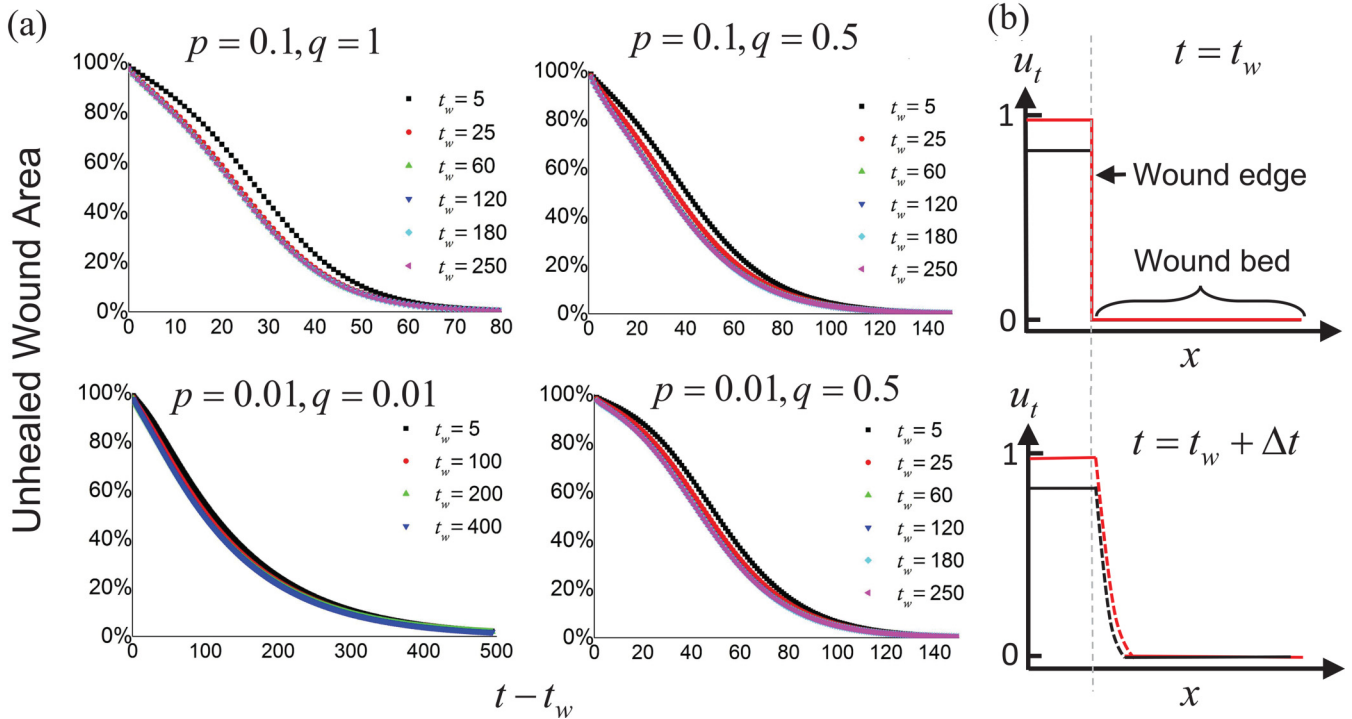

FIG. 13. Time-delayed wound healings in the original reaction-diffusion model. (a) Healing results for different waiting periods under various parameter settings. The meaning of p and q is explained in Appendix B 2. (b) The cell density distribution after wounding for two healing events at different cell densities immediately after wounding (the red line for higher density and the black line for lower density). The vertical axis is the cell density u_t and the horizontal axis is the cell position x. The grey dashed line marks the position of the wound edge immediately after wounding and the space to the right of the grey dashed line is the wound bed with zero cell density. Top: the distribution of cell density at t_w immediately after wounding. Bottom: the distribution at $t_w + \Delta t$ (Δt is a small-time interval). Higher cell density on the wound edge at t_w causes more cells to migrate into the wound bed (the red line is always above the black line).
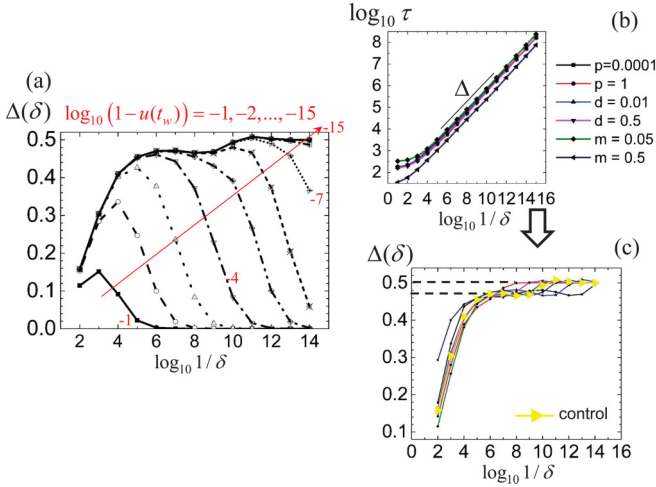
FIG. 14. The critical exponent estimated from numerical results of asymmetric reaction-diffusion equation (ARDE). $\Delta(\delta_i) = [\log_{10}\tau(\delta_{i+1}) - \log_{10}\tau(\delta_{i-1})]/(\log_{10}\delta_{i+1} - \log_{10}\delta_{i-1})$ denotes the derivatives of $\log_{10}\tau$ as a function of delay fraction δ calculated from a series of data $\tau(\delta_i), i = 1, 2 \ldots, N$. (a) $\Delta(\delta)$ under various wounding densities $u(t_w)$ with the parameter setting $m = d = 1, p = 0.01$ (corresponding to the data in Fig. 7). (b) Divergence of $\log_{10}\tau$ with other parameter settings under high contact inhibition $u(t_w) = 1 - 10^{-15}$. (c) $\Delta(\delta)$ calculated from the data in (b) in comparison with the control group ($m = d = 1, p = 0.01$).

2. Critical exponent β

In the ARDE models, the divergence of healing time τ as a function of $1/\delta$ follows a power-law relation $\tau \sim (1/\delta)^{\beta}$ when $u(t_w)$ is extremely close to a saturation value of 1 (maximal contact inhibition). To evaluate the value of β, we calculated the local derivatives of $\ln\tau$ as a function of delay fraction δ from a series of data $\tau(\delta_i), i = 1, 2 \ldots N$ with $\delta_{i+1}/\delta_i = 0.1$ [corresponding to Fig. 7(a) in the main text] as $\Delta(\delta_i) = [\log_{10}\tau(\delta_{i+1}) - \log_{10}\tau(\delta_{i-1})]/(\log_{10}\delta_{i+1} - \log_{10}\delta_{i-1})$ [Fig. 14(a)]. The value of $\Delta(\delta)$ has three regimes with the increase in $\ln\delta^{-1}$: $\Delta(\delta)$ rises from zero first, then encounters a plateau, and finally returns to zero. For small $u(t_w)$ (low contact inhibition), the regime with a stable plateau, which indicates a power-law relation $\tau \sim (1/\delta)^{\beta}$, is absent; for $u(t_w)$ extremely close to 1 (high contact inhibition), the stable regime exhibits two subregimes with the first plateau roughly at $\beta = \Delta(\delta) = 0.469 \pm 0.002$ and the second one at 0.5. We confirmed the existence of such a staircase in the plateau regime with various model parameters under $u(t_w) = 1 - 10^{-15}$ [Figs. 14(b) and 14(c)], where the first plateau is universally around $\beta = \Delta(\delta) = 0.471 \pm 0.009$, yet the onset timings of the second plateau [$\beta = \Delta(\delta) = 0.5$] are diverse. Meanwhile, the data groups with smaller p, smaller d, and larger m tend to exhibit longer first plateaus, implying that the first plateau with lower β is more associated with the mitotic or reaction term in ARDE; by contrast, if the diffusional dynamics is dominant (larger p, larger d, and smaller m), the second plateau ($\tau \sim \sqrt{1/\delta}$) will quickly ensue.

Clarifying the origin of this phenomenon by relating it to some established universality class might shed light on the application of existing physics models or lead to the discovery of a class of criticality related to complicated life phenomena. We expect future studies on the mapping between the ARDE (which is originally designed for a biological process) and a physical model (such as the kinetically constrained model [53]) to elaborate this criticality.

3. Vanishing of aging with a large waiting time

In the ARDE model for wound healing, the increase in healing time τ with waiting time t_w was bounded by a ceiling where τ stops diverging and the aging effect vanishes. This is because when cell density saturates ($u \to 1$), the number of diffusing cells $\nabla[D(u)\nabla u]$ from the wound edge immediately after wounding converges to a nonzero value $[D(u \to 1) + D(u \to 0)]/4$, asymptotically. The small number of cells migrating from the wound edge to the wound bed as an instant response to wounding is independent of $u(t_w)$ in the long time limit:

$$\frac{du}{dt} = \nabla(D(u)\nabla u) \sim \frac{1}{4}[D(u \to 1) + D(u \to 0)] \approx \frac{2p+1}{4(p+1)}.$$

Therefore, the instantaneous recovery of $M(u)$ for cells in the wound bed converged to a nonzero rate when the waiting time approached infinity as follows:

$$dM(t_w)/dt = dM[u(t_w)]/dt = \delta du(x^{\text{wound}}, t)/dt$$
$$= \delta(2p+1)/4(p+1).$$

This leads to a vanishing of aging effect [$dM(u)/dt$ irrelevant to t_w]. Such a ceiling for criticality is almost inevitable in models where cell movement is driven by any existent density differences, even if in the following extremal circumstances:

(i) The diffusivity recovers in a delayed pace such that $D(t) = \gamma D_{\text{con}}[u(t)] + (1 - \gamma)D(t - \Delta t)$, where $D_{\text{con}}(u)$ can be any ideal diffusivity purely under contact inhibition at cell density u satisfying (ii), and γ, ranging from 0 to 1, is the delay fraction imposed on the diffusion term;

(ii) $D_{\text{con}}(u \to 1) > 0$ and converges to zero with $D_{\text{con}}(0) = 1$.

The reason can be demonstrated as follows: The instantaneous number of cells that migrate into the wound immediately after wounding depends on two terms, $D(u \to 1)$ and $D(u \to 0)$, representing the cell diffusivity on the wound edge and in the wound bed, respectively. Even if $D(u \to 1)$ (at the edge) approaches zero with large waiting time t_w, $D(u = 0, t_w + \Delta t)$ can asymptotically converge to a minimum of nonzero value in the long time limit as

$$\gamma D_{\text{con}}(u \to 0) + (1 - \gamma)D(t_w \to \infty)$$
$$= \gamma D_{\text{con}}(u \to 0) + (1 - \gamma)D(u \to 1)$$
$$\approx \gamma D_{\text{con}}(0) + (1 - \gamma)D_{\text{con}}(1),$$

which is not sensitive to large t_w. Clearly, the onset of the ceiling regime and the vanishing of aging effect at extremely large waiting times is inevitable for the ARDE models. We postulate that in real experiments, incomplete healing may occur with such long waiting times (see Appendix C 3).

TABLE II. Adapted from Table II in Lou and Chen [46]. Discrete receptor dynamics for any single cell at time step t. The denotations R_g, R_E, R_h, R_a, R_d represent the amount of growth receptors, ECM receptors, adhesion receptors, arrest receptors, and death receptors, respectively. The denotation E is the concentration of ECM substances. The receptor and ECM amount change dynamically for each cell. The values of the parameters are listed in Table III.

Conditions		Cell behaviors		Receptor dynamics
$R_g + R_h < R_M$ AND not arrested		grow		$R_g[t+1] = (1+\gamma)R_g[t]$
				$E[t+1] = sR_g[t] - c(R_h[t]+R_a[t]+R_d[t])$
None		adhere to neighbors		$R_h[t+1] = R_h[t] + \Delta R_h[t]$
		and ECM		$R_E[t+1] = R_E[t] + \Delta R_E[t]$
				$R_g[t+1] = R_g[t] - \Delta R_h[t] - \Delta R_E[t]$
				see ΔR_h and ΔR_E in Appendixes A and B
				in Lou and Chen [46]
$R_h > p$ AND $R_E > e$		polarize		$R_a[t+1] = R_a[t] + a_{\text{scr}}R_h[t]$
				$R_h[t+1] = (1-a_{\text{scr}})R_h[t+1]$
$R_h \leqslant p$ OR $R_E \leqslant e$		not polarize		$R_d[t+1] = R_d[t] + d_{\text{scr}}(R_h[t]+R_a[t])$
				$R_h[t+1] = (1-d_{\text{scr}})R_h[t]$
				$R_a[t+1] = (1-d_{\text{scr}})R_a[t]$
Not arrest	$R_a > a$	restriction point		entry into arrest
Arrest	$R_a \leqslant a$ AND $R_g > g$			exit from arrest
$R_g + R_h < R_M$ AND not arrested		proliferate	empty	seed a daughter cell at a random vacant neighboring site
				$R_g{}^{\text{daughter}}[t+1] = R_g[t+1] = B$
			no space	doing nothing
$R_d > d$		suicide		$R_*[t+1] = 0, E[t+1] = 0$
				R_* refers to all kinds of receptors
$R_h + R_E < h$		move		See Appendix C in Lou and Chen [46]

APPENDIX C: WOUND HEALINGS BY DISCRETE RECEPTOR DYNAMICS MODEL (DRDM)

1. Model and parameter settings

DRDM is an on-grid cell-based model for epithelial tissue formation. Each cell is equipped with five types of receptors: growth receptor, adhesion receptor, ECM receptor, arrest receptor, and death receptor. The cell compares the number of receptors with different receptor thresholds to trigger a series of decision-making processes that will update the configuration of these five receptor types (Table II). Thus, the number of receptors always dynamically changes, determining the functions and the phenotype of a cell. Interested readers can refer to Lou and Chen [46] for a detailed demonstration of the model construction and the receptor dynamics.

The parameters involved in the receptor dynamics for wound healing simulations are summarized in Table III. Here we explain the meaning of adhesion threshold (the meaning of other key thresholds is introduced in the main text, Sec. III B). Adhesion threshold h: if the total number of adhesion and ECM receptors is below the adhesion threshold—i.e., the adhesive cohesion is low enough—cells can move to an empty neighboring site with a lesser amount of surrounding ECM. We should mention that a time step in the simulation using the parameter settings in Table III is roughly one-quarter of the cell doubling time. The nonproliferative spreading cells at the forefront of the edge are not modeled by DRDM because proliferation and migration may simultaneously occur in one time step if the receptor configuration of a cell meets the specific conditions as is described in Table II.

2. Snapshots of healings

The snapshots of healings with three different waiting times are illustrated in Fig. 15, where the slowdown of healing can be observed.

3. Heterogeneous healing rates and incomplete healing phenomena

The most eminent discrepancy between the agent-based model DRDM and the ARDE model lies in the ability to reproduce the heterogeneous healing rates at the leading edge and the incomplete healing phenomenon. In the ARDE model, the varying ability of cell proliferation and migration depends only on the cell density, suggesting that the cells have the potential to grow and move [$D(u) > 0$, $M(u) > 0$] as long as any unhealed space with cell density $u < 1$ remains. By contrast, in the DRDM, the inhibition of cell growth and cell mobility depends not only on cell density, but also on the adherent cohesion among cells, the sensitivity to ECM, and on the intrinsic regulation for cell cycle arrest. These sophisticated factors yield a huge diversity of cell phenotypes in DRDM, resulting in heterogeneous healing behaviors along the wound edge. As shown in Figs. 16(a) and 16(b), some of the leading cells invade into the wound bed quickly while others remain inactive, producing some finger-shaped healing fronts. Although the macroscopic cell mitotic rate averaged along the whole edge should be equivalent to $M(u)$ in the ARDE model, this equivalence holds only for smaller waiting times when more cells are viable with less heterogeneous cell phenotypes.

The heterogeneity among cell phenotypes profoundly affects the healing processes when the waiting time is long

TABLE III. Parameter settings used for time-delayed wound healing simulations in Fig. 9(a). Note that we set death threshold d as a sufficiently large number to ensure that cell death was negligible during the whole simulation. ECM threshold e and growth threshold g were two variables scanned from 0 to $2R_M$ with a sampling interval of $0.05R_M$. For the simulations in Fig. 9(b), g was fixed as $0.05R_M$ and e as $0.8R_M$. The simulation space was a rectangular space with the 71 columns and the 10,000 rows. The wound bed was a rectangular space with 16 columns and 10 000 rows located at the center of the space.

Parameter	Definition	Baseline value
S	space size of the 2D normal lattice with periodical boundary condition	71×10000
W	size of the wound bed	16×10000
B	number of basic growth receptors for a newly born cell	30
R_M	minimum of total receptor numbers for mitosis	100
s	secretion rate of ECM	10
c	decrease rate of ECM	0.5
g	growth threshold	from 0.0 to $2.0R_M$
p	polarization threshold	$0.09\,R_M$
h	adhesion threshold	$0.2\,R_M$
d	death threshold	$10^9\,R_M$
e	ECM threshold	from 0.0 to $2.0R_M$
a	arrest threshold	$3\,R_M$
γ	growth rate of growth receptor concentration	0.1
a_{scr}	accumulation rate of arrest receptor	0.25
d_{scr}	accumulation rate of death receptor	0.5
e_{scr}	upper limit number of ECM secreted by per mass of growth receptors	20

enough, causing incomplete healings in DRDM especially with a low arrest threshold a, i.e., a higher tendency for cell-cycle arrest. As a result, healing was totally ceased in the middle of the process [Fig. 16(c)], leaving the wound areas

unhealed. To understand this phenomenon, one can imagine an extremely unfortunate case where no cell on the wound edge is reactivated to proliferate or move. This occurs when very few cells are active in the system with a finite number of
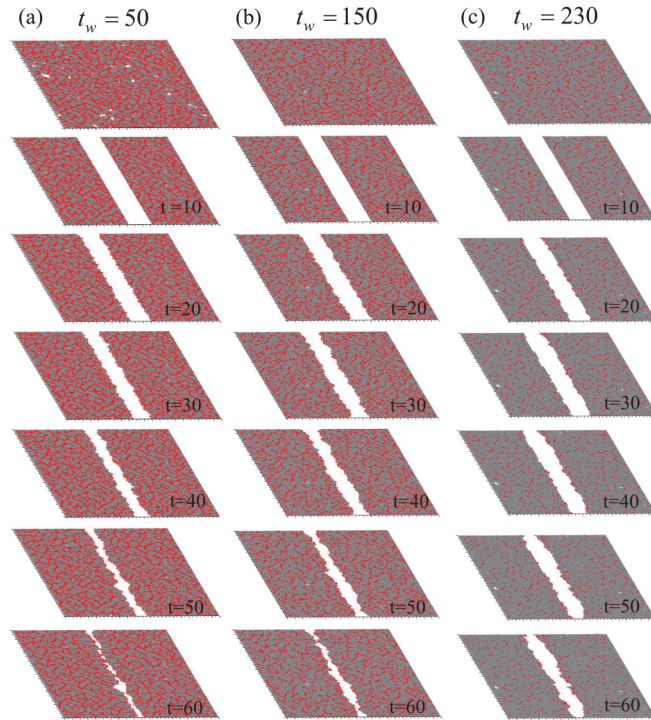

FIG. 15. Snapshots of simulated time-delayed wound healings in discrete receptor dynamics model (DRDM) with low diffusivity. Each grey dot represents one arrested cell, while the red one is for a proliferating cell. ECM threshold $e = 2.5R_M$, arrest threshold $a = 0.2R_M$, growth threshold $g = 0.1R_M$, adhesion threshold $h = 0$ (zero motility). Other parameters are the same as in Table II.
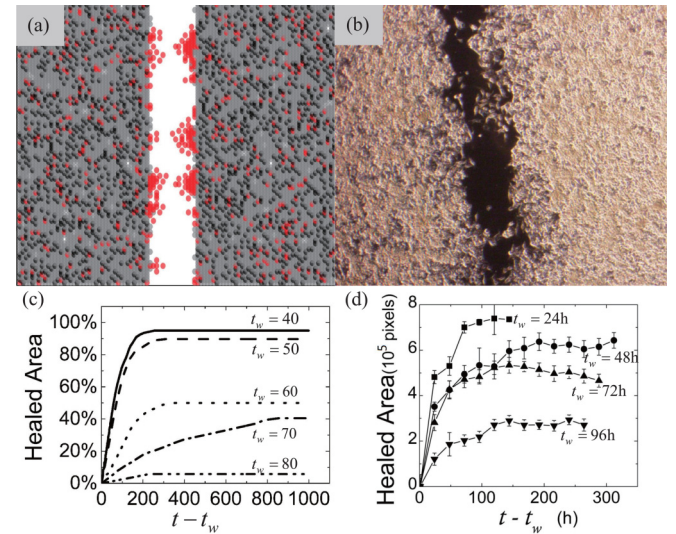

FIG. 16. Finger-shaped healing fronts and incomplete healing phenomena. (a) One snapshot from discrete receptor dynamics model (DRDM) simulations. Red dots: proliferating cells; grey dots: temporarily arrested cells; black dots: permanently arrested cells. Note that nonproliferative spreading cells at the forefront of the edge are not modeled in DRDM simulation. (b) One snapshot from experiment I. The snapshot size was 100×100, and wound bed size was 16×100. (c) Incomplete healing events in DRDM, with arrest threshold $a = 0.15R_M$, extracellular matrix (ECM) threshold $e = 2.5R_M$ and growth threshold $g = 0.3R_M$. Other parameters are the same as listed in Table II. (d) Incomplete healings *in vitro* with HepG2.2.15 cells subcultured for about 40 generations.
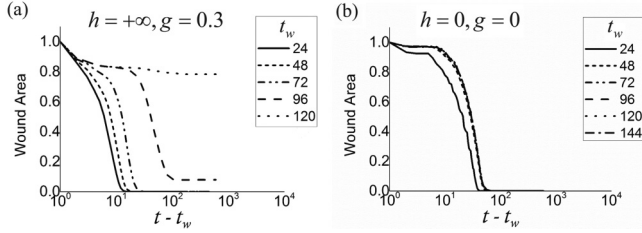
FIG. 17. Wound closure in the discrete receptor dynamics model (DRDM). (a) Free cell movement ($h \rightarrow \infty$) with a high regrowth barrier ($g = 0.3 R_M$). (b) No cell movement ($h = 0$) with low regrowth barrier ($g = 0$).

total cells, hence the averaged mitotic rate along the edge can only decrease in a quantum manner with longer waiting times: jumping from a small value to zero. Even if the finger-shaped edges can form, a lower value of arrest threshold a, which indicates strong inhibition of cell cycle, will gradually suppress the mitosis of the cells during the healing, thus preventing the cells at the "finger" from further invasion into the denuded area.

In fact, we also observed incomplete healings in another series of experiment with a cell line of HepG2.2.15 subcultured for about 40 generations, i.e., these cells were "old" in contrast to the newly thawed cell line used in experiments I and II (in the main text). The reason of incomplete healing *in vitro* is unclear so far; however, we postulate that the accumulation of the damages to the cells over generations can correspond to the decrease in arrest thresholds in the DRDM simulation. Accordingly, the incomplete healing may be caused by the strong cell-cycle inhibition in experiments and it should occur for two kinds of cells: (1) the old cells which inherently have low arrest thresholds; (2) the newly thawed cells with extremely long waiting time, which have higher arrest thresholds but accumulate excessive nondegradable "arrest receptors" over time.

4. Time delayed healing in DRDM under varied adhesion thresholds

The effect of delayed recovery in cell movement can also be examined in DRDM by varying adhesion threshold h, which represents the minimum level of adhesion required to fix a cell in its local surroundings. In Fig. 17(a), the adhesion threshold h was set to infinity, indicating that cell movement is totally free regardless of any cell-cell or cell-ECM adhesion. Meanwhile, the growth threshold g was set as $0.3 R_M$ which is a huge barrier for the cells to re-enter the growth state from an arrest state. The results revealed that even with the freest cell movement, a strong regrowth barrier still causes the slowdown of healing for short waiting times and the incomplete healing for longer waiting times. Conversely, if h is 0, which means zero cell motility due to a strong cell-cell and cell-ECM adhesion, a small value of g could still ensure a quick healing process, as shown in Fig. 17(b), nevertheless, with the cliff-shaped healing curves. This comparison illustrates that the role of mitotic deterioration is much more significant than that of retarded cell movement in reproducing the slowdown of healing in DRDM. Besides, we clearly see that the reduced cell motility causes a
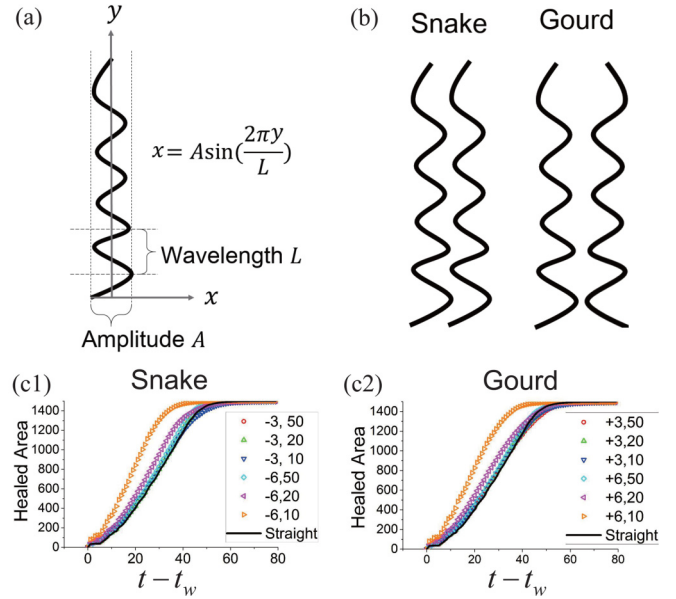

FIG. 18. Wound healing *in silico* with curved wound edges. (a) Wave models of the wound geometry. (b) Two types of wound bed geometry. (c) Simulation results. Each legend for the scattering dot is characterized by a set of parameters, denoted as $\pm A, L$ in the figure, where the minus (positive) sign stands for snake-shape (gourd-shape) wound bed, A is the amplitude of the wound edge wave, and L is the wavelength.

"frozen" phase before the initiation of healing in Fig. 17(b). This also implies that in the early stage of healing, the slow cell migration postpones the initiation of cell proliferation that follows. However, the "frozen" phase and cliff-shaped healing curves cannot be seen from the experiment; hence it is very unlikely for the cells to have low motility with a high proliferation rate in the real situation.

APPENDIX D: WOUND EDGE ROUGHNESS

The increase in cell-cell cohesive bonds with time led to irregularly zigzagged wound edges in all experiments, even if the wound edges were intended to be straight. Whether this unevenness of the wound edges have introduced artificial biases on the healing rates in experiments needs to be examined.

1. Edge roughness in DRDM

We first established a model for controllable curvatures of the wound edge as illustrated in Fig. 18(a), where a wave function mimics the nonstraight wound edge with a specific amplitude A and wavelength L. Hence, the unevenness of the wound edge can be quantified by A/L. Additionally, we considered two types of curved wound bed [Fig. 18(b)]: a snakelike bed (two paralleled wound edges) and a gourdlike bed (two mirror-symmetric wound edges). The simulation results in Fig. 18(c) show that a higher value of A/L leads to more rapid healing, whereas the straight wound edge heals most slowly. No significant differences were detected between snake-shaped [Fig. 18(c1)] and gourd-shaped [Fig. 18(c2)] wound beds.

2. Edge roughness in experiments

Agreeing with the conclusions of another study (refer to Arciero *et al.* [35]), our data *in silico* suggested a crucial phenomenon: wounds with highly curved edges can heal quickly. To clarify whether the nonstraight wound edges indeed introduced mechanical confounders into the experiments, we perform an analysis of the curvature of real wound gaps in experiments. As the edge curvatures in the experiments were irregular, we calculated the *roughness* instead of the curvature of the edge.

The line edge *roughness* is related to the fractal dimension of a line [54,55] and is indicated by the scaling exponent α in the local standard deviation $G(r) = r^{\alpha}$ of a wound edge line with respect to the local window width r. The local standard deviation of the edge fluctuations can be calculated as follows:

$$G(r) = \frac{1}{N-r} \sum_{j=1}^{N-r} \left[\frac{1}{r+1} \sum_{i=j}^{j+r} \left(x_i - \frac{1}{r+1} \sum_{k=j}^{j+r} x_k \right)^2 \right]^{1/2}$$

$$r = 0, 1, \ldots, N-1,$$

where $\{x_i\}_{i=1,2,\ldots,N}$ is the set of horizontal positions of the N evenly sampled points at the wound edge along the vertical axis [see Fig. 19(a)]. The sample interval is 25/3 microns, which is roughly a cell diameter and the sample point number $N = 73$ for each edge in the snapshots.

When the exponent α is 1, the edge is perfectly straight; if α is close to zero, the line is highly rough. Figure 19(b) presents four examples of different wave functions distinguished by their respective geometry and *roughness*. Using these four wave functions of the wound edge in DRDM simulations, we can plot the relationship between the healing time and *roughness* α as shown in Fig. 19(c), where the healing time first rises rapidly when α is close to zero, and then increases mildly when $\alpha > 0.4$. This plot implies that the healing rate is not so sensitive to the edge geometry unless the edge is extremely rough. Figure 19(d) shows the local standard deviation $G(r)$ of eight exemplar edges in experiment I. Figure 19(e) displays the average wound edge *roughness* for each group (dotted circles) with typical individual samples (open squares) outlining the variance. Overall, no significant difference in wound edge roughness could be identified.
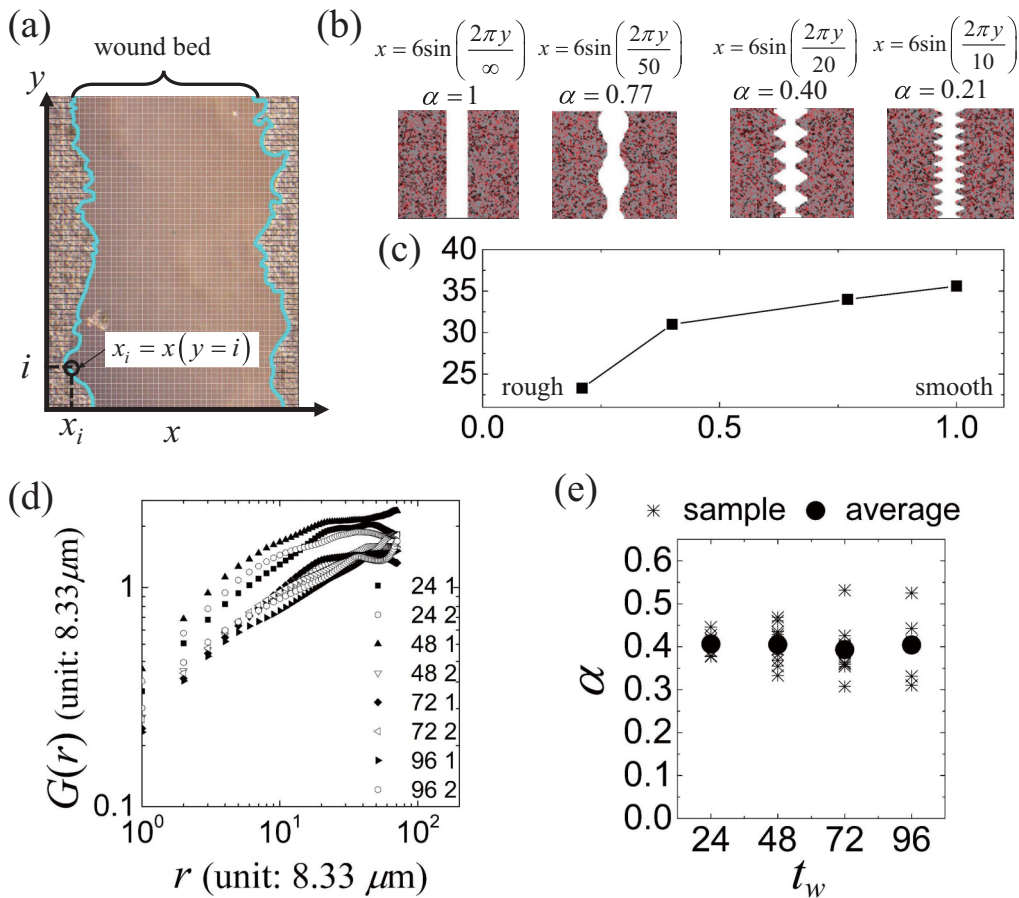

FIG. 19. Edge roughness in discrete receptor dynamics model (DRDM) simulations and *in vitro* experiments. (a) The method of calculating roughness exponent. In a newly set x-y coordinate system, the wound edge (outlined in light green) was evenly sampled along y axis as the points coordinated by the vertical positions $y_i = i$ and the correspondent horizontal positions $x_i (i = 1, 2, \ldots N)$. The sample interval is 25/3 microns and the total number of sample points N is 73. The local standard deviation $G(r)$ was then calculated based on a series of $\{x_i\}$ and fitted to r^{α}, where r is the window width and α is the indicator for line edge *roughness*. (b) Roughness exponent α calculated for four wave functions aligned with their wound bed geometries. (c) Healing time vs roughness exponent α in DRDM simulation using four wave functions presented in (b). (d) Local standard deviation $G(r)$ for eight exemplar edges from experiment I. (e) Comparison of averaged line roughness among four groups in experiment I, labeled by their waiting times (which are 24, 48, 72, and 96 h).

Notwithstanding that the variances were large in some groups, the absolute values of α were still within the range from 0.30 to 0.50. According to Fig. 19(c), these rough edges resulted in limited even negligible impact on healing efficiency. In conclusion, we argue that the irregular curvatures of wound geometry caused by increasing intercellular adhesion did not bias the healing processes with different waiting times in our *in vitro* experiments.

APPENDIX E: SPATIAL DISTRIBUTION OF CELL PHENOTYPES DURING WOUND HEALING

Wound healing is a complex process consisting of cell spreading, cell proliferation, and cell migration. The spatial distribution of these cellular events behind the wound edge is essential for the modeling of the wound healing process.

According to Haider *et al.* [56], the mitotic rate of cells was evaluated by laser scanning cytometry that the percentage of cells at the S phase in the wound region is over tenfold larger than that outside of the wound region. Similar results can be found in other literature [57–59]. Ronot *et al.* [60] used optical flow analysis to quantitatively measure the cell velocity in relation to the distance from the wound center for three kinds of cell lines (murine fibroblasts, human epithelioid HeLa cells, and rat rhabdomyosarcoma cells) and found that the velocity of the migratory cells peaked at the wound edge and then decayed exponentially with the distance from the edge.

Zahm *et al.* [28] used immunofluorescent staining technique to quantitatively investigate the spatial distribution of spreading, migrating, and proliferating cells behind the wound edge for respiratory epithelial cells. It is clearly shown that
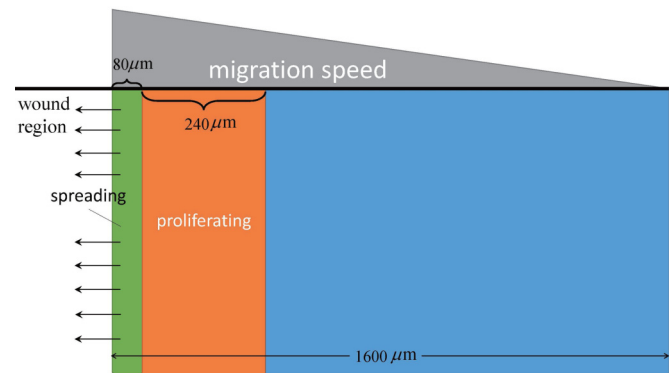

FIG. 20. Spatial distribution of spreading, proliferation and migrating cells behind the wound edge in wound healing for *in vitro* respiratory epithelial cells. Information was extracted from the data shown in Ref. [28].

the cells right at the front rows of the wound edge were nonproliferative spreading cells around which the lamellipodia was formed to pull the whole cell sheet into the wound region. Near the wound edge (80–320 microns behind the wound edge), almost 50% of the cells were proliferative; while far behind the wound edge (>300 microns), the percentage of the proliferative cells abruptly decreased to less than 5%. In contrast, the migratory ability of cells was strongest at the wound edge and decayed as the distance from the wound edge increases (0–1600 microns behind the edge). Figure 20 illustrates the spatial distribution of spreading, proliferation, and the cell migratory ability during the wound healing for respiratory epithelial cells *in vitro*. Similar results can also be found in Savla *et al.* [61].

[1] C. López-Otín, M. A. Blasco, L. Partridge, M. Serrano, and G. Kroemer, Cell **153**, 1194 (2013).
[2] K. Sousounis, J. A. Baddour, and P. A. Tsonis, Curr. Top. Dev. Biol. **108**, 217 (2014).
[3] J. Coffman, S. Rieger, A. Rogers, D. Updike, and V. Yin, Regen. Med. **1**, 16003 (2016).
[4] C. B. Harley, A. B. Futcher, and C. W. Greider, Nature (London) **345**, 458 (1990).
[5] J. C. Jeyapalan and J. M. Sedivy, Mech. Ageing Dev. **129**, 467 (2008).
[6] I. M. Conboy, M. J. Conboy, A. J. Wagers, E. R. Girma, I. L. Weissman, and T. A. Rando, Nature (London) **433**, 760 (2005).
[7] C. E. Muller-Sieburg, H. B. Sieburg, J. M. Bernitz, and G. Cattarossi, Blood **119**, 3900 (2012).
[8] L. C. E. Struik, Ph.D. thesis, Delft University of Technology, 1977.
[9] J.-P. Bouchaud, L. F. Cugliandolo, J. Kurchan, and M. Mezard, in *Spin Glasses and Random Fields*, edited by A. P. Young (World Scientific, Singapore, 1998).
[10] B. Abou, D. Bonn, and J. Meunier, Phys. Rev. E **64**, 021510 (2001).
[11] M. Nicodemi and A. Coniglio, Phys. Rev. Lett. **82**, 916 (1999).
[12] G. Lenormand, A. M. Alencar, X. Trepat, E. H. Zhou, B. Fabry, J. P. Butler, and J. J. Fredberg, in *Phase Transitions in Cell Biology* (Springer, Amsterdam, 2008), pp. 111–141.

[13] P. C. Hohenberg and B. I. Halperin, Rev. Mod. Phys. **49**, 435 (1977).
[14] M. Henkel, H. Hinrichsen, S. Lübeck, and M. Pleimling, *Nonequilibrium Phase Transitions* (Springer, Berlin, 2008), Vol. 2.
[15] J. P. Bouchaud, J. de Physique I **2**, 1705 (1992).
[16] T. E. Angelini, E. Hannezo, X. Trepat, M. Marquez, J. J. Fredberg, and D. A. Weitz, Proc. Natl. Acad. Sci. USA **108**, 4714 (2011).
[17] M. Sadati, N. T. Qazvini, R. Krishnan, C. Y. Park, and J. J. Fredberg, Differentiation **86**, 121 (2013).
[18] M. Sadati, A. Nourhani, J. J. Fredberg, and N. Taheri Qazvini, Sys. Biol. Med. **6**, 137 (2014).
[19] A. F. Pegoraro, J. J. Fredberg, and J. A. Park. Exp. Cell Res. **343**, 54 (2016).
[20] L. Berthier and J. Kurchan, Nat. Phys. **9**, 310 (2013).
[21] D. Bi, X. Yang, M. C. Marchetti, and M. L. Manning. Phys. Rev. X **6**, 021011 (2016).
[22] S. Garcia, E. Hannezo, J. Elgeti, J. F. Joanny, P. Silberzan, and N. S. Gov, Proc. Natl. Acad. Sci. USA **112**, 15314 (2015).
[23] C. G. Rolli, H. Nakayama, K. Yamaguchi, J. P. Spatz, R. Kemkemer, and J. Nakanishi, Biomaterials **33**, 2409 (2012).
[24] P. Martin, Science **276**, 75 (1997).
[25] C. C. Liang, A. Y. Park, and J. L. Guan, Nat. Protoc. **2**, 329 (2007).

[26] J. E. Jonkman, J. A. Cathcart, F. Xu, M. E. Bartolini, J. E. Amon, K. M. Stevens, and P. Colarusso, Cell Adh. Migr. **8**, 440 (2014).

[27] R. Riahi, Y. Yang, D. D. Zhang, and P. K. Wong, J. Lab. Autom. **17**, 59 (2012).

[28] J. M. Zahm, H. Kaplan, A. L. Hérard, F. Doriot, D. Pierrot, P. Somelette, and E. Puchelle, Cell Motil. Cytoskeleton **37**, 33 (1997).

[29] P. K. Maini, D. S. McElwain, and D. Leavesley, Appl. Math. Lett. **17**, 575 (2004); Tissue Eng. **10**, 475 (2004).

[30] M. J. Simpson, K. A. Landman, B. D. Hughes, and D. F. Newgreen, J. Theor. Biol. **243**, 343 (2006).

[31] A. Tremel, A. Cai, N. Tirtaatmadja, B. D. Hughes, G. W. Stevens, K. A. Landman, and A. J. O'Connor, Chem. Eng. Sci. **64**, 247 (2009).

[32] A. Q. Cai, K. A. Landman, and B. D. Hughes, J. Theor. Biol. **245**, 576 (2007).

[33] M. J. Simpson, C. Towne, D. L. S. McElwain, and Z. Upton, Phys. Rev. E **82**, 041901 (2010).

[34] J. Arciero and D. Swigon, in *Complex Systems and Computational Biology Approaches to Acute Inflammation* (Springer, New York, 2013), pp. 185–207.

[35] J. C. Arciero, Q. Mi, M. Branca, D. Hackam, and D. Swigon, Wound Repair Regen. **21**, 256 (2013).

[36] A. Ravasio, I. Cheddadi, T. Chen, T. Pereira, H. T. Ong, C. Bertocchi, A. Brugues, A. Jacinto, A. J. Kabla, Y. Toyama *et al.*, Nat. Commun. **6**, 7683 (2015).

[37] E. Khain, M. Katakowski, N. Charteris, F. Jiang, and M. Chopp, Phys. Rev. E **86**, 011904 (2012).

[38] N. Charteris and E. Khain, New J. Phys. **16**, 025002 (2014).

[39] R. A. Fisher, Ann. Eugen. **7**, 355 (1937).

[40] A. Kolmogorov, I. Petrovsky, and N. Piskunov, Moscow Univ. Math. Bull. **1**, 1 (1937).

[41] J. A. Sherratt and J. D. Murray, Proc. Biol. Sci. **241**, 29 (1990).

[42] M. Reffay, M. C. Parrini, O. Cochet-Escartin, B. Ladoux, A. Buguin, S. Coscoy, F. Amblard, J. Camonis, and P. Silberzan, Nat. Cell Biol. **16**, 217 (2014).

[43] O. Cochet-Escartin, J. Ranft, P. Silberzan, and P. Marcq, Biophys. J. **106**, 65 (2014).

[44] E. Anon, X. Serra-Picamal, P. Hersen, N. C. Gauthier, M. P. Sheetz, X. Trepat, and B. Ladoux, Proc. Natl. Acad. Sci. USA **109**, 10891 (2012).

[45] S. R. K. Vedula, G. Peyret, I. Cheddadi, T. Chen, A. Brugues, H. Hirata, H. Lopex-Memendez, Y. Toyama, L. N. Almeida, X. Trepat, and C. T. Lim, Nat. Commun. **6**, 6111 (2015).

[46] Y. Lou and Y. Chen, J. Theor. Biol. **404**, 15 (2016).

[47] C. Monthus and J.-P. Bouchaud, J. Phys. A **29**, 3847 (1996).

[48] M. Henkel and M. Pleimling, Europhys. Lett. **76**, 561 (2006).

[49] M. E. Carlson, M. Hsu, and I. M. Conboy, Nature (London) **454**, 528 (2008).

[50] B. Novak, J. J. Tyson, B. Gyorffy, and A. Csikasz-Nagy, Nat. Cell Biol. **9**, 724 (2007).

[51] A. Bürkle, M. Moreno-Villanueva, J. Bernhard, M. Blasco, G. Zondag, J. H. Hoeijmakers, O. Toussaint, B. Grubeck-Loebenstein, E. Moccheqiani, S. Collino *et al.*, Mech. Ageing Dev. **151**, 2 (2015).

[52] K. Christensen, T. E. Johnson, and J. W. Vaupel, Nat. Rev. Genet. **7**, 436 (2006).

[53] F. Ritort and P. Sollich, Adv. Phys. **52**, 219 (2003).

[54] A. L. Barabási and H. E. Stanley. *Fractal Concepts in Surface Growth* (Cambridge University Press, Cambridge, England, 1995).

[55] V. Constantoudis, G. P. Patsis, L. H. A Leunissen, and E. Gogolides, J. Vac. Sci. Technol. B **22**, 1974 (2004).

[56] A. S. Haider, J. Grabarek, B. Eng, P. Pedraza, N. R. Fereri, E. A. Balazs, and Z. Darzynkiewicz, Cytometry **53**, 1 (2003).

[57] G. D. Winter, *Epidermal Wound Healing* (Year Book Medical Publishers, Chicago, 1972).

[58] J. Bereiter-Hahn, *Epidermal Cell Migration and Wound Repair*, edited by J. Bereiter-Hahn, A. G. Matoltsy, and K. S. Richards (Springer, Berlin, Heidelberg, 1986), pp. 443–471.

[59] T. Schreier, E. Degen, and W. Baschong, Res. Exp. Med. **193**, 195 (1993).

[60] X. Ronot, A. Doisy, and P. Tracqui, Cytometry **41**, 19 (2000).

[61] U. Savla, J. Appl. Physiol. **96**, 566 (2004).